

waveOrder: generalist framework for label-agnostic computational microscopy

TALON CHANDLER^{1,*}, EDUARDO HIRATA-MIYASAKI¹, IVAN E. IVANOV¹, ZIWEN LIU¹, DEEPIKA SUNDARRAMAN¹, ALLYSON QUINN RYAN¹, ADRIAN JACOBO¹, KEIR BALLA¹, AND SHALIN B. MEHTA^{1,*}

¹Chan Zuckerberg Biohub San Francisco, San Francisco, USA

*Correspondence: talon.chandler@czbiohub.org, shalin.mehta@czbiohub.org

Compiled December 16, 2024

Correlative computational microscopy is accelerating the mapping of dynamic biological systems by integrating morphological and molecular measurements across spatial scales, from organelles to entire organisms. Visualization, measurement, and prediction of interactions among the components of biological systems can be accelerated by generalist computational imaging frameworks that relax the trade-offs imposed by multiplex dynamic imaging. This work reports a generalist framework for wave optical imaging of the architectural order (waveOrder) among biomolecules for encoding and decoding multiple specimen properties from a minimal set of acquired channels, with or without fluorescent labels. waveOrder expresses material properties in terms of elegant physically motivated basis vectors directly interpretable as phase, absorption, birefringence, diattenuation, and fluorophore density; and it expresses image data in terms of directly measurable Stokes parameters. We report a corresponding multi-channel reconstruction algorithm to recover specimen properties in multiple contrast modes. With this framework, we implement multiple 3D computational microscopy methods, including quantitative phase imaging, quantitative label-free imaging with phase and polarization, and fluorescence deconvolution imaging, across scales ranging from organelles to whole zebrafish. These advances are available via an extensible open-source computational imaging library, waveOrder, and a napari plugin, recOrder.

1. INTRODUCTION

Biological functions emerge from the interaction of many components that span length scales, i.e., biomolecules, organelles, cells, tissues, and organs. Correlative imaging of these components' physical and molecular properties is a growing area of microscopy. Computational imaging methods that optically encode multiple physical and molecular properties and decode them computationally are particularly promising as they relax the trade-offs between spatial resolution, temporal resolution, number of channels, field of view, and sample health that constrain multiplex dynamic imaging.

Correlative label-free and fluorescence imaging "fills the vacuum" of observing a few fluorescent molecules in complex biological environments. These approaches enable measurement of conserved physical properties of cellular compartments [1] and enable dynamic high-throughput imaging for mapping responses of multiple organelles to complex perturbations [2]. Such correlative datasets have enabled the development of neural networks that virtually stain molecular labels from label-free contrast modes [3–5], further improving the ability to analyze interactions among organelles and cells. Light-sheet fluorescence

microscopy has long been used to measure the dynamic interactions of cells [6] and organelles [2, 7]. At scales larger than organelles, recent methods for spatial mapping of gene expression [8], protein distribution [9], and gene perturbations [10] use multi-channel imaging systems that encode multiple molecular species in the imaging data. At the finer scale of biomolecular complexes, cryo-CLEM (correlative light and electron microscopy) reveals the structural basis of the biomolecular function [11, 12].

The microscopy methods used by the above technologies can be modeled via linear image formation models, even though they rely on diverse light-matter interactions. The visualization, measurement, and analysis of specimen properties in these biological studies can be improved by developing a computational imaging framework that reconstructs specimen properties from the acquired multi-channel imaging data. This paper describes a computational imaging framework that addresses this need.

2. BACKGROUND AND PRIOR WORK

Many works describe microscopic image formation for individual contrast modes including fluorescence contrast [13, 14],

phase and absorption contrast [15, 16], and polarization-resolved birefringence contrast [17, 18]. Recently, multiple papers have developed computational imaging methods for integrative measurements of specimen properties, but with models specific to label-free contrast [3, 19–21] or fluorescence contrast [22, 23]. The waveOrder framework unifies and extends these models to *multi-contrast* and *multi-channel* imaging systems that include scalar and polarization-resolved imaging with or without fluorescence labels.

The most general image formation models account for statistical fluctuations in the electric field of light, i.e., coherence, and how the coherence is modulated due to propagation or interaction with matter. Modeling coherence requires bilinear functions (functions whose output depends on pairs of points in the imaging path) and propagation of second-order statistics [15, 24–28]. We start with this approach before restricting our attention to imaging problems that can be modeled with linear functions. Specifically, we consider spatially incoherent fluorescence samples and label-free imaging systems with a spatially incoherent source.

Several existing frameworks provide some, but not all, of the features of waveOrder. Deconvolution libraries typically focus on fluorescence deconvolution [29, 30], limiting their value in multi-channel correlative settings. Differentiable microscopy libraries [31, 32] flexibly model a wide variety of imaging systems to enable new designs and reconstructions, but they don't often provide generalist inverse algorithms applicable to diverse contrast mechanisms. waveOrder prioritizes linear reconstruction models for the most widely used computational microscopy contrast methods, facilitating broad applications.

We also find that many reconstruction implementations are not used broadly for biological research because they are not reproducible or easy to access. waveOrder is an open-source and actively developed project that attempts to maximize the usability and impact of linear computational imaging methods by unifying and maintaining the most valuable reconstruction techniques in biological microscopy. waveOrder leverages PyTorch for cross-platform, high-performance analysis of large datasets and integration with learned computer vision models.

In our view, this paper makes the following contributions

- a simulation and reconstruction framework that can be applied to linear microscopy contrast modes, including fluorescence, phase, absorption, birefringence, and diattenuation;
- clear links between material properties, their light-matter interactions, and the mathematical operators that represent them;
- a demonstration of reconstructions of simulated phantoms, physical phantoms, and biological samples across length scales; and
- demonstrates reconstructions across the scales of organelles, cells, organs, and organisms using a PyTorch-based library.

3. WAVEORDER FRAMEWORK

We start by describing a framework for reconstructing material properties from microscopic imaging data. By representing material properties and data as vectors, we describe our reconstructions as the solution to an optimization problem. Using broadly applicable assumptions of linearity, shift invariance, and weak scattering, we describe all contrasts as the result of

banks of point spread functions. We describe the physics behind the major contrast mechanisms and compute their transfer functions from illumination, scattering, and detection models. Throughout, we use carefully chosen basis functions to enable the physical interpretation of light and material properties. We describe all notation as we introduce it, and we collect all symbols in Section 10.

A. Objects and data as vectors, imaging as an operator

We represent a biological sample as a series of *volumetric maps of material properties*, shown schematically in Figure 1a, i. For example, a cell might be approximately described by two fluorophore density maps, $f_1(\mathbf{r}_o)$ and $f_2(\mathbf{r}_o)$ where \mathbf{r}_o is a 3D object position vector, one map for each of two different fluorophores that label biological structures of interest, and a density map $\rho(\mathbf{r}_o)$. Three maps are unlikely to describe the sample completely, so we generalize and collect any number of volumetric maps into a single vector

$$\mathbf{f} = [f_1, f_2, f_3, \dots]^T = [f_1(\mathbf{r}_o), f_2(\mathbf{r}_o), \rho(\mathbf{r}_o), \dots]^T, \quad (1)$$

which represents all of the properties of our sample.

When we image our sample in a microscope, we arrange for the material properties to be encoded into a list of *volumetric datasets*, each called a *channel*, shown schematically in Figure 1a, ii. For example, we might use a fluorescence light path to encode fluorophore density maps into two channels, $d_1(\mathbf{r}_d)$ and $d_2(\mathbf{r}_d)$ where \mathbf{r}_d is a 3D detector position vector, then we can change to a transmission light path to encode the density $\rho(\mathbf{r}_o)$ into the third channel $d_3(\mathbf{r}_d)$. Similar to our object properties, we collect any number of channels into a single vector

$$\mathbf{d} = [d_1, d_2, d_3, \dots]^T = [d_1(\mathbf{r}_d), d_2(\mathbf{r}_d), d_3(\mathbf{r}_d), \dots]^T, \quad (2)$$

which represents all of the data we collect from our sample.

We can represent the imaging process with a single *forward operator* \mathcal{H} that encodes the material properties \mathbf{f} into measured volumetric datasets \mathbf{d}

$$\mathbf{d} = \mathcal{H}\mathbf{f} + \mathbf{b}, \quad (3)$$

where \mathbf{b} is a spatially uniform background in each channel. Note that \mathcal{H} might encode multiple material properties into a single channel. For example, the material properties of phase and anisotropy can be jointly encoded into several label-free data channels.

B. Reconstructing object properties

We would like to recover as much as we can about the object's material properties \mathbf{f} from the measured data \mathbf{d} , but we are faced with a major problem—the *forward operator* \mathcal{H} is *never invertible*. There are always object properties that are invisible to the imaging system, and one way to find invisible properties is to make the properties smaller than the resolution limit of the imaging system. For example, if we have a visible-light microscopy dataset \mathbf{d} there are an infinite number of molecular-scale configurations that could result in the same dataset, so we have no hope of choosing a single \mathbf{f} as *the* true measured properties.

We need to choose a single set of material properties from among the infinite possible solutions that agree with the data—a *reconstruction problem*. Our strategy is to choose the material properties that minimize a scalar objective function $Q(\mathbf{f}, \mathbf{d})$

$$\hat{\mathbf{f}} = \mathcal{R}\mathbf{d} = \underset{\mathbf{f}}{\operatorname{argmin}} Q(\mathbf{f}, \mathbf{d}), \quad (4)$$

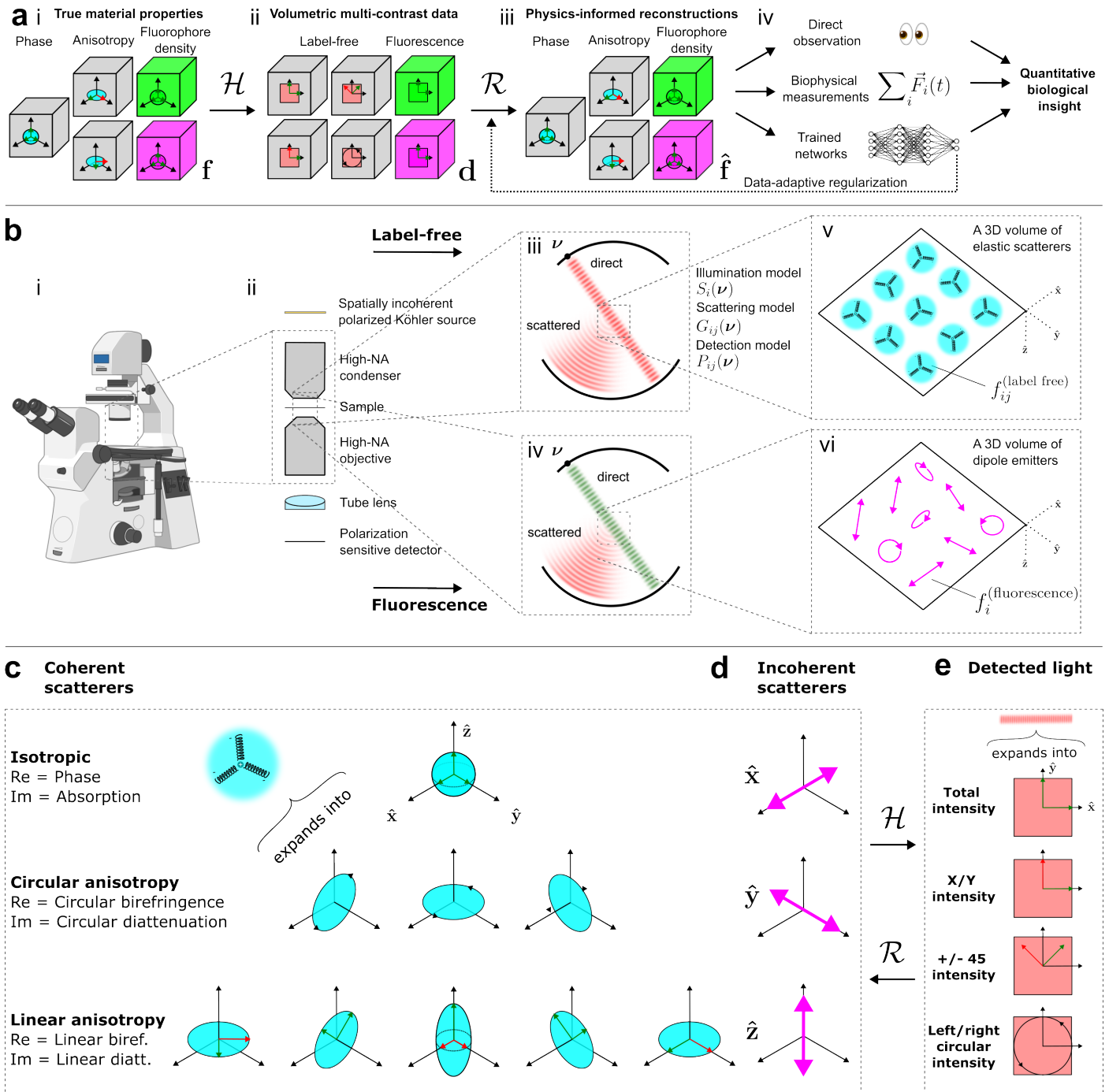


Fig. 1. A framework for volumetric microscopy of phase, absorption, birefringence, diattenuation, fluorescence density, and fluorescence orientation. (a) Microscopes encode (i) true material properties into (ii) multi-contrast multi-channel volumetric datasets by changing spectral and polarization illumination and detection filters. Physics-informed models of the encoding process, \mathcal{H} , lead to physics-informed reconstruction operators, \mathcal{R} , that enable (iii) reconstructions of underlying material properties. (iv) We find that physics-informed reconstructions are useful for improving performance on downstream observation, biophysical, and learned tasks. (b) We model the encoding process of an (i) off-the-shelf inverted microscope stand outfitted with (ii) an incoherent source, variable spectral and polarization filters, and a polarization-sensitive detector. Two classes of contrast are available: label-free contrast where (iii) direct fields scatter coherently from the sample and direct-scatter interference generates contrast, and (iv) fluorescence contrast where direct fields that excite inelastic-scattering fluorophores are filtered so that scatter-scatter interference generates contrast. We model coherent scatterers as (v) a volume of scattering potential tensors that model the relationship between incident electric fields and induced dipole moments. We model inelastic fluorescence scatterers as (vi) a volume of dipole emission moments. Both coherent and incoherent dipoles can be linear, circular, and elliptical, though fluorescent dipoles used in biological microscopy are primarily linear. (c) Expanding the scattering potential tensor onto spherical harmonic tensors enables interpretation in terms of phase, absorption, birefringence, and diattenuation. (d) Expanding dipole emitters into Cartesian components with complex coefficients enables interpretation of single emitters' orientations. (e) Expanding measurable data into Stokes parameters enables modeling of all possible polarization measurements. See also Video 1.

where the argmin notation means that we choose as our solution $\hat{\mathbf{f}}$ the \mathbf{f} that minimizes the value of $Q(\mathbf{f}, \mathbf{d})$. One choice is the *least-squares objective* $Q^{(\text{ls})}(\mathbf{f}, \mathbf{d}) = \|\mathbf{d} - \mathbf{b} - \mathcal{H}\mathbf{f}\|_2^2$, but this solution tends to amplify noise. A better choice is a *Tikhonov-regularized least-squares objective*

$$Q_\eta^{(\text{tls})}(\mathbf{f}, \mathbf{d}) = \|\mathbf{d} - \mathbf{b} - \mathcal{H}\mathbf{f}\|_2^2 - \eta \|\mathbf{f}\|_2^2, \quad (5)$$

which adds a regularization parameter η that suppresses the size of the solution \mathbf{f} , an example of a *prior* that penalizes large solutions. Many other objective functions are possible, including those that include physics-informed and learned priors.

After choosing an objective function, the minimization problem needs to be solved, an often challenging task. Fortunately, if \mathcal{H} is linear then the Tikhonov-regularized least-squares objective can be minimized in a single step described in **Supplement 14**, generating efficient noise-tolerant estimates of material properties, **Figure 1a, iii**.

As illustrated in **Figure 1a, iv**, physics-informed reconstruction operators prepare raw microscopy data for improved direct visual inspection, improved biophysical estimates [1], and improved performance on tasks performed by trained networks [5]. Therefore, the next sections develop physically interpretable models of light-matter interactions for diverse contrast modes.

C. Contrast modes

We model the image formation process of an off-the-shelf inverted microscope stand (**Figure 1b, i-ii**) outfitted with a spatially incoherent Köhler source with variable polarization filters, variable spectral filters, a high-NA condenser and objective, and an imaging path that includes a polarization-sensitive detector.

All contrast is formed by illuminating the sample with electric fields that scatter from the sample then interfere on the detector. If we consider only single scattering events, the *first Born approximation*, then we can rewrite **Equation 3** as

$$\mathbf{d} = \left| \mathcal{S}\mathbf{f} + \mathbf{e}^{(\text{d})} \right|^2, \quad (6)$$

where \mathcal{S} is a *scattering operator* that models the scattered fields that reach the detector and $\mathbf{e}^{(\text{d})}$ models the unscattered *direct fields* that reach the detector. Expanding the square reveals four terms

$$\mathbf{d} = |\mathcal{S}|^2 |\mathbf{f}|^2 + \mathbf{e}^{+(\text{d})} \mathcal{S}\mathbf{f} + \mathbf{f}^\dagger \mathcal{S}^\dagger \mathbf{e}^{(\text{d})} + |\mathbf{e}^{(\text{d})}|^2, \quad (7)$$

that we refer to as the scatter-scatter, scatter-direct, direct-scatter, and direct-direct terms, respectively, and \dagger denotes conjugate transpose.

We consider two classes of contrast. *Label-free contrast* (**Figure 1b, iii**) is generated by illuminating the sample with light that interacts with the sample *coherently*—that is, scattered fields have the same wavelength and a fixed phase relationship with the illuminating fields. When a plane wave encounters a coherent scatterer, the oscillating electric field accelerates bound electrons in the scatterer, and these accelerated charges generate spherical scattered fields. The direct and scattered fields interfere and generate contrast via the scatter-direct and direct-scatter terms. The direct-direct term creates a uniform background, and for *weakly scattering* samples the scatter-scatter term is small and ignorable. Therefore, label-free contrast is generated by the direct-scatter and scatter-direct terms on top of a direct-direct background. Finally, each point on the source emits incoherently, so we can treat each source point individually and find the complete contrast pattern by *summing over the source*.

Fluorescence contrast (**Figure 1b, iv**) is generated by illuminating fluorescent scatterers and imaging their scattered light. Fluorescent scatterers are *incoherent*, so the scattered fields have a random phase at a longer wavelength than the illuminating fields. Therefore, the scatter-direct and direct-scatter terms do not generate contrast, so the only way to measure sample-dependent contrast is via the small scatter-scatter term. Fortunately, the direct and scattered fields are at different wavelengths, so the direct fields can be filtered with minimal bleedthrough. Therefore, fluorescence contrast is generated by the scatter-scatter term with a direct-direct bleedthrough background. Finally, fluorescent scatterers emit incoherently, so we can find the complete contrast pattern by *summing over the sample*.

Both label-free and fluorescence contrast modes can generate additional contrast from *anisotropic samples*. Label-free samples can be anisotropic if the scatterer's bound electrons accelerate anisotropically. We illustrate a label-free anisotropic sample schematically as an electron bound to its nucleus by springs of varying spring constant (**Figure 1b, v**). When polarized light is incident on an anisotropic sample, it accelerates the bound electrons in linear, circular, or elliptical *dipoles*, which emit anisotropic polarized light in patterns that encode the orientation of the induced electron motion and the underlying anisotropy of the scatterer. Therefore, information about the sample's label-free anisotropy is encoded in the polarization and intensity pattern of the detected light. Similarly, fluorescent scatterers emit along linear, circular, or elliptical dipoles (**Figure 1b, vi**), though linear dipoles are most common among the fluorophores used in biological microscopy.

D. Physically interpretable basis functions

When we illuminate a label-free sample, the 3D induced dipole moment is the product of the incident field and a 3×3 matrix called the *permittivity tensor* [21, 28]. By convention, we change to a unitless quantity and subtract the isotropic background (**Supplement 15**) to arrive at a complete set of label-free sample properties—the complex-valued 3×3 matrix called the *scattering potential tensor*, $f_{ij}^{(\text{lf})}$. Each entry of the scattering potential tensor can be interpreted directly (e.g. the complex-valued $f_{xz}^{(\text{lf})}$ is the relative magnitude and phase of the x component of the dipole induced by a z -oriented field), but this interpretation can be challenging to understand physically. To improve physical interpretability, we expand the scattering potential tensor onto the *spherical harmonic tensors*, a set of nine 3×3 matrices whose complex-valued expansion coefficients can be directly interpreted in terms of phase, absorption, birefringence, and diattenuation. We schematize each of these spherical harmonic tensors in **Figure 1c** by drawing each tensor's eigenvalues and eigenvectors, and we describe the spherical harmonic tensor basis in detail in **Supplement 15**.

In a fluorescent sample, the 3D emission dipole moment can be represented by a three-component vector $f_i^{(\text{fl})}$ (**Figure 1d**) with real-valued coefficients for purely linear dipoles and complex-valued coefficients for arbitrary dipoles. Contrast arises from the scatter-scatter term, so our measurements are proportional to the squares of the dipole components $|f_i^{(\text{fl})}|^2$.

For dynamic ensembles of fluorescent emitters, the measurements are proportional to the *second-moment matrix* $\langle f_i^{(\text{fl})} f_j^{*(\text{fl})} \rangle$ [13, 22, 33]. Similar to the scattering potential tensor, we can expand the second-moment matrix onto the spherical harmonic tensors, but here we interpret the coefficients in terms

of orientation distribution functions [14, 23].

Finally, we express our data in terms of the *Stokes parameters*, a set of four real-valued parameters that are physically interpretable as the intensities measured behind various polarizing filters. The Stokes parameters can also be interpreted as the coefficients of the electric field's second-moment matrix expanded onto the *Pauli matrices* (Figure 1e, Supplement 16).

E. Linear contrast-separable shift-invariant imaging systems

Under approximations that are applicable to a wide range of microscopes (details in Section 5 and Supplement 17), we can model our imaging system by splitting our material properties, data channels, and forward model into independent groups called *contrast modes*, e.g. one label-free mode and several fluorescence modes. Each of these contrast modes is approximately linear across object properties, and each property-to-channel mapping is approximately spatially linear and shift invariant. Therefore, we can express our imaging model as

$$d_c^{(m)}(\mathbf{r}_d) = \sum_p \int d\mathbf{r}_o h_{cp}^{(m)}(\mathbf{r}_d - \mathbf{r}_o) f_p^{(m)}(\mathbf{r}_o) + b_c^{(m)}, \quad (8)$$

where m indexes contrast modes, p indexes material properties, c indexes data channels, and $h_{cp}^{(m)}$ is a bank of *point spread functions* that model the entire multi-contrast multi-channel imaging system. We can reexpress this relationship in the Fourier domain as

$$D_c^{(m)}(\mathbf{v}) = \sum_p H_{cp}^{(m)}(\mathbf{v}) F_p^{(m)}(\mathbf{v}) + b_c^{(m)} \delta(\mathbf{v}). \quad (9)$$

where \mathbf{v} is a 3D spatial frequency coordinate, capital letters denote 3D Fourier transforms, and $H_{cp}^{(m)}(\mathbf{v})$ is a bank of *transfer functions* that model the transmission of spatial frequency components through the imaging system. We inspect the properties of these transfer functions next.

F. Summary of transfer functions

The waveOrder framework calculates all transfer functions from three core submodels:

1. an illumination model—the vector source pupil $S_i(\mathbf{v})$,
2. a scattering model—the Green's tensor spectrum $G_{ij}(\mathbf{v})$,
3. a detection model—the tensor detection pupil $P_{ij}(\mathbf{v})$.

All three submodels are expressed as complex-valued spherical shell functions with radius $1/\lambda$ in the frequency domain, where λ is the wavelength in the imaging media.

The Green's tensor spectrum is particularly important for modeling anisotropic contrast. Linear dipole moments emit polarized light in a doughnut-shaped intensity pattern (Figure 2a), and the Green's tensor spectrum (Figure 2b) efficiently models all dipole emitters (coherent or incoherent; linear, circular, or elliptical dipoles in any orientation) with a single function.

All transfer functions can be expressed as products and auto-correlations of the illumination, scattering, and detection models, see Table 1 and Supplement 17. We refer to the complete transfer functions as *vector models* because they account for the complete vectorial nature of light and dipole scattering. We also include scalar models that ignore vector effects, which are reasonable approximations when unpolarized illumination and unpolarized detection are used on isotropic samples.

Figures 2c–f show the support and phase of several examples of waveOrder's transfer functions. We briefly highlight several key features

- vector models consist of a grid of transfer functions, one for each data channel and material property,
- scalar models consist of a single transfer function, and
- we model real-valued data, so our transfer functions are *Hermitian*, that is $H_{cp}^{(m)}(\mathbf{v}) = H_{cp}^{*(m)}(-\mathbf{v})$.

4. MULTI-CONTRAST MULTI-CHANNEL RECONSTRUCTIONS ACROSS LENGTH SCALES

A. Label-free simulated and real test specimen

We tested our newly developed anisotropic label-free model on polarization-diverse data acquired from a laser-etched anisotropy phantom with transverse radially anisotropic bubbles arranged in a spoke pattern (Figure 3a,i). We measured four volumetric Stokes datasets (Figure 3a,ii) and applied waveOrder's reconstruction algorithm to estimate three label-free material properties that correspond to phase and transverse birefringence (Figure 3a,iii).

In parallel, we simulated the anisotropic phantom (Figure 3b,i) and the image formation process (Figure 3b,ii), then we applied an identical reconstruction algorithm to estimate material properties (Figure 3b,iii). Figures 3a, ii–ii and b,ii–iii can be directly compared to indicate the quality of our models, where differences can arise from imperfect modeling of both the object and the image formation process. While our simulations recreate the most important contrast features, the real measurements have contrast with a broader axial extent and poorer transverse spatial resolution than our simulations—likely due to imperfections in our phantom and slightly aberrated imaging.

We compared an earlier ray-optics based voxel-by-voxel reconstruction algorithm [3] with waveOrder's new wave optical reconstruction algorithm Figure 3c. We find that wave-optical reconstructions yield marginally improved transverse resolution Figure 3d measured via transverse modulation transfer functions from azimuthal profiles, and denoised and defocus-symmetric axial profiles Figure 3e. We also observe orientation reversals between spokes, reconstruction artifacts that are analogous to well-known negative ringing artifacts in fluorescence deconvolution.

B. Cells and tissues

We applied waveOrder reconstructions to multi-channel data acquired from samples across length scales. Figure 4 shows alternating columns of data and reconstructions for transverse birefringence, phase, and fluorescence density. In data acquired from A549 cells (Figure 4a) we observe improved sectioning, denoising, and contrast in phase and reconstructed fluorescence properties compared to their raw-data counterparts (Figure 4a, ii–iii). In the orientation channel (Figure 4a, i) we observe marginal improvements in contrast, but generally poor performance with reduced SNR and suppression of features that are apparent in the raw data. We attribute some of the performance drop to our imperfect noise model—we reconstruct from non-Gaussian Stokes parameters which is at odds with our Tikhonov least-squares reconstruction algorithm. Additionally, we have not explored the interaction between our Stokes-based background correction and our wave-optical reconstructions, another likely area for improvement.

We acquired multi-contrast data from an entire living zebrafish (Figure 4b), then reconstructed fluorescence density, phase, and birefringence from specific regions of interest (Figure

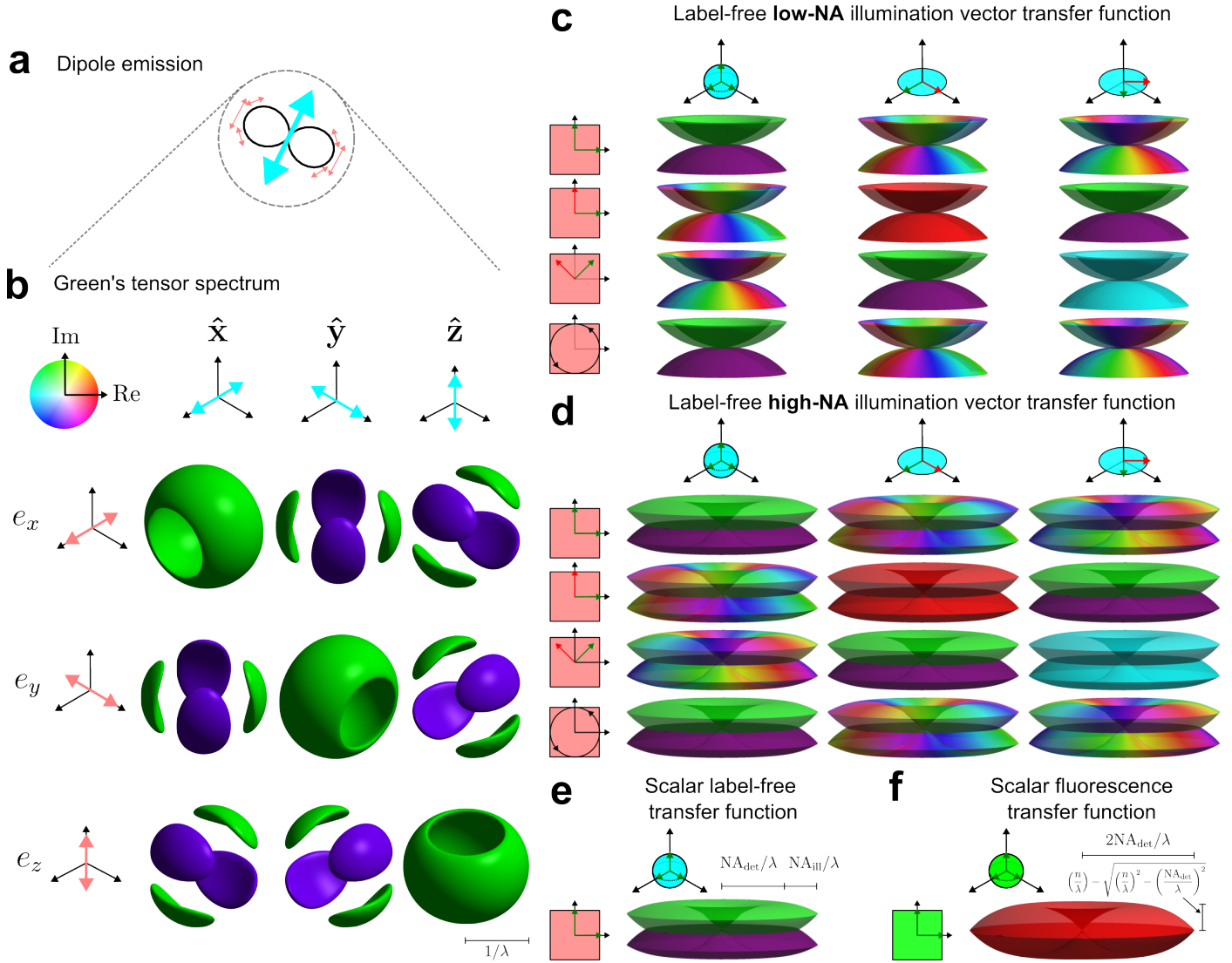


Fig. 2. Key components of the forward model. (a) A dipole emitter (blue arrow) emits polarized fields (red arrows) in an anisotropic pattern (black line, radius proportional to power). (b) Arbitrary linear, circular, and elliptical dipole emissions can be modeled with the Green's tensor spectrum $G_{ij}(\mathbf{v})$. Each surface shows the quarter-maximum intensity of on-shell spectral field components (rows) e_x , e_y , and e_z emitted by dipoles oriented along (columns) \hat{x} , \hat{y} , and \hat{z} , with relative phase shown in color (see color rose). Orthogonal slices through the Green's tensor spectrum and the Green's tensor are shown in **Supplement Figure 8**. (c–f) 3D support of various transfer functions with phase encoded in color. (c–d) Real label-free vector transfer functions with $NA_{\text{det}} = 0.75$ and circularly polarized illumination that expresses polarization-resolved data (rows) as outputs of filters that modulate material properties (columns) with (c) low-NA illumination $NA_{\text{ill}} = 0.1$ and (d) high-NA illumination $NA_{\text{ill}} = 0.5$. (e) Scalar label-free transfer function with $NA_{\text{ill}} = 0.5$ and $NA_{\text{det}} = 0.75$. (f) Scalar fluorescence transfer function with $NA_{\text{det}} = 0.75$. See also **Video 2**.

	vector	scalar
label-free	$\begin{bmatrix} H_{cp}^{(\text{lf, re})}(\mathbf{v}) \\ H_{cp}^{(\text{lf, im})}(\mathbf{v}) \end{bmatrix} = \sigma_c^{ii'} \begin{bmatrix} 1 & 1 \\ i & -i \end{bmatrix} \begin{bmatrix} [P_{ij}G_{jn} \star P_{i'k'}S_{k'}S_k^*](\mathbf{v}) \\ [P_{ik'}S_{k'}S_k^* \star P_{ij}G_{jn}](\mathbf{v}) \end{bmatrix} \mathcal{Y}_p^{nk}$	$\begin{bmatrix} H^{(\text{lf, re, s})}(\mathbf{v}) \\ H^{(\text{lf, im, s})}(\mathbf{v}) \end{bmatrix} = \begin{bmatrix} 1 & 1 \\ i & -i \end{bmatrix} \begin{bmatrix} [P \star PS](\mathbf{v}) \\ [PS \star P](\mathbf{v}) \end{bmatrix}$
fluorescence	$H_{cp}^{(\text{fl})}(\mathbf{v}) = \sigma_c^{ii'} [P_{ij}G_{jk} \star P_{i'j'}G_{j'k'}](\mathbf{v}) \mathcal{Y}_p^{kk'}$	$H^{(\text{fl, s})}(\mathbf{v}) = [P \star P](\mathbf{v})$

Table 1. Transfer functions for different contrast modes (rows) and optical models (columns) expressed in terms of the illumination model S , the scattering model G , the detection model P , the object-space basis \mathcal{Y} , and the data-space basis σ . Sums over i, i', j, j', k and k' are implied.

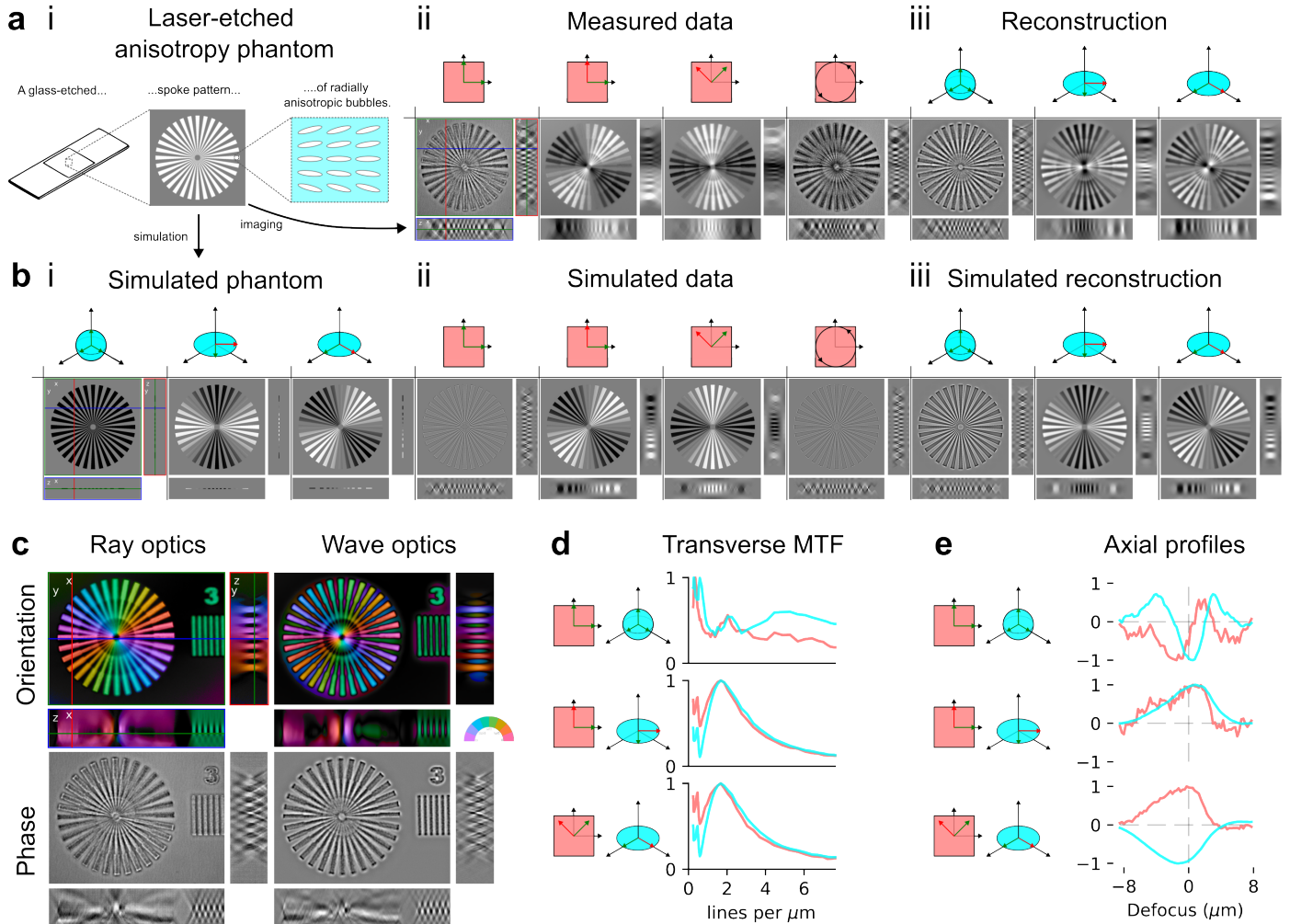


Fig. 3. Demonstration of vectorial multi-channel reconstruction with experiment and simulation. We imaged **(a) (i)** a laser-etched spoke pattern of transverse radially anisotropic bubbles. **(ii)** We made volumetric measurements of the Stokes parameters (columns), and applied a multi-channel label-free reconstruction to **(iii)** recover material properties. **(b)** We **(i)** simulated the phantom's material properties, **(ii)** simulated the imaging process, then **(iii)** simulated the reconstruction. **(c)** We encoded transverse birefringence properties into color, where brightness indicates the strength of the anisotropy and hue indicate the slow-axis orientation. We compared the orientation and phase reconstructions (rows) in ray- and wave-optics reconstructions (columns). **(d)** For each data and material property, we measured a series of azimuthal profiles at different radii on the spoke pattern and used the 10th–90th percentile modulation as an empirical estimate of the transverse modulation transfer function (MTF). **(e)** Similarly, we measured axial profiles through each data and material property. See also **Video 3**.

4c–e). We observe improved sectioning, denoising, and contrast in all three reconstructions. For example, in the label-free **Figure 4i, c–e** we see improved contrast between the gut and muscles, and in the fluorescence channels **Figure 4iii, c–e** we see improved contrast and resolution of immune cells. Improved contrast in the zebrafish gut (bottom of **Figure 4c**) is particularly valuable for tracking immune-cell dynamics encoded in the fluorescence reconstructions.

C. Choice of regularization parameter

waveOrder’s physics-informed reconstructions rely on a list of fixed parameters that specify imaging conditions (e.g., numerical apertures, wavelength, voxel sizes) and a single regularization parameter η , which penalizes large solutions and suppresses noise. Though principled ways to choose regularization parameters exist [34, 35], in practice, it is common to inspect a regularization sweep and choose an empirical solution (for example, **Figure 5** and **Supplement Figure 6**). Regularization parameters that are too small result in noisy reconstructions, while regularization parameters that are too large result in blurry reconstructions. Additionally, we find that the transverse mid-band power, the power in transverse spatial frequencies between one-eighth and one-quarter of the cutoff, is a useful scalar metric that can indicate high-quality reconstructions—see the plateau in **Figure 5(d)**.

waveOrder’s current design uses a single regularization parameter per contrast mode. For example, we use one regularization parameter for each fluorescence deconvolution, one for each phase-from-brightfield reconstruction, and one for each joint reconstruction of phase and orientation. These single-parameter Tikhonov-regularized least squares reconstructions assume that all measured channels have an SNR proportional to their intensity and that the physical model accurately describes the differences in intensity between channels. This requirement becomes challenging when reconstructing directly from Stokes parameters, typically estimated with varying SNR. For example, the Stokes parameters that preceded the reconstruction in **Figure 5** include a very noisy S_3 . Here, we dropped S_3 from our dataset, ignoring its small contribution, but improved reconstructions with channel-specific regularization parameters may allow us to use this channel more effectively.

In future work, we are excited to pursue data-adaptive and channel-adaptive regularization in a data- and task-dependent manner. We are especially excited by methods that can address model mismatch, which often limits the quality of our reconstructions. For example, while **Figure 5(iii,b–e)** shows improved contrast and sectioning, model mismatch limits the quality of our reconstructions by leaving artifactual double cones throughout the reconstruction, particularly visible as transverse rings from bright out-of-focus cells.

5. LIMITATIONS

While waveOrder enables the development of image formation models and reconstruction algorithms for a wide variety of computational microscopy techniques, its current design makes the following assumptions that are not valid in certain applications:

- **consistent SNR in all channels**, which assumes that all data channels that encode a given contrast have a similar signal-to-noise ratio.
- **channel linearity**, which excludes non-linear crosstalk between channels e.g. FRET, strongly scattering samples,

- **spatial linearity**, which excludes saturation of fluorescent samples or the camera,
- **shift invariance**, which excludes shift-variant point spread functions,
- **weak, single scattering**, which excludes thick multiply scattering samples, e.g. older zebrafish and thick tissue slices,
- **aberration-free imaging**, which excludes applications in the presence of sample-induced aberrations.
- **contrast-separable imaging**, which excludes crosstalk between label-free and fluorescence contrast modes.

6. DISCUSSION AND CONCLUSION

waveOrder improves on earlier multi-channel correlative imaging methods in several ways. Compared to LC-PolScope reconstruction methods [36], waveOrder uses a wave-optical approach that reconstructs from diffraction-limited groups of voxels instead of reconstructing voxel by voxel. waveOrder also extends quantitative label-free imaging with phase and polarization (QLIPP) [3], by using a vectorial wave-optics model of multiple specimen properties, not just phase. waveOrder also extends permittivity tensor imaging (PTI) [21], which reconstructs only uniaxial permittivity tensors while waveOrder is compatible with arbitrary biaxial materials. The waveOrder framework also generalizes previous work on imaging polarized fluorescence ensembles [14, 23], where diffraction-limited ensembles of fluorescent dipoles reduce to orientation distribution functions. As discussed earlier, we view careful noise handling and more robust background correction as areas for future work.

To conclude, we find that linear models provide a strong framework for widely applicable computational microscopy techniques, including phase, absorption, birefringence, diattenuation, and anisotropic fluorescence imaging. We find the waveOrder framework useful for understanding, simulating, and reconstructing data acquired with this class of techniques, and we demonstrate its ability to improve multi-contrast multi-channel data across length scales.

7. DATA AND CODE AVAILABILITY

Demos, data and code can be found in the [recOrder](#) and [waveOrder](#) repositories.

8. ACKNOWLEDGEMENTS

We thank [Shashvat Mehta](#) for developing the animation shown in **Video 1**. We thank the Scientific Computing Platform at CZ Biohub for enabling high-performance reconstructions.

9. FUNDING

All authors are supported by intramural funding from Chan Zuckerberg Biohub, San Francisco, an institute funded by the Chan Zuckerberg Initiative. We thank Priscilla Chan and Mark Zuckerberg for supporting the CZ Biohub Network.

REFERENCES

1. R. Schlüßler, K. Kim, M. Nötzel, *et al.*, “Correlative all-optical quantification of mass density and mechanics of subcellular compartments with fluorescence specificity,” *eLife* **11**, e68490 (2022). Publisher: eLife Sciences Publications, Ltd.

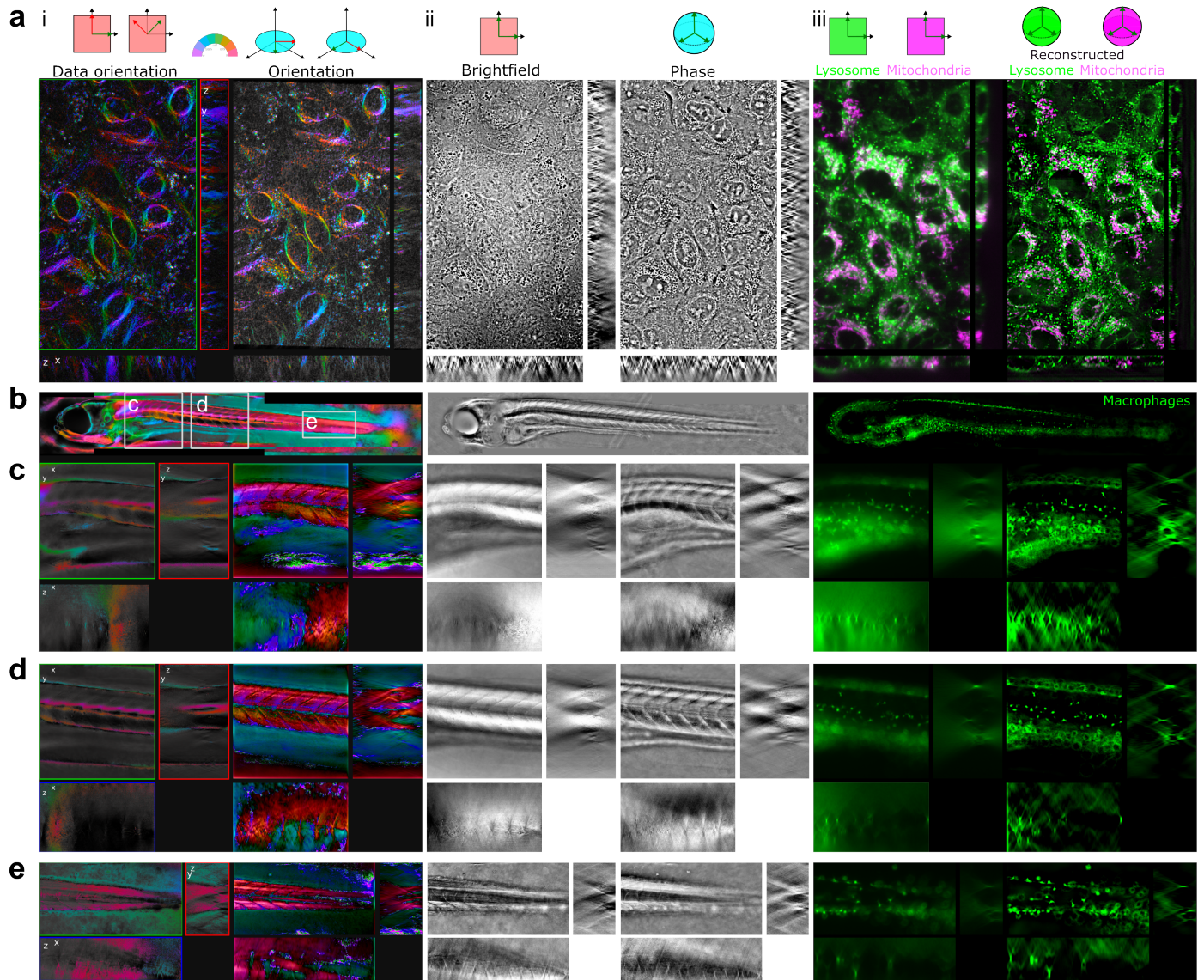


Fig. 4. Reconstructions improve visualization and interpretation across length scales in (a) A549 cells, (b) zebrafish, and (c–e) zebrafish regions of interest. (i) Orientation data (left) and reconstructions (right). (ii) Brightfield data (left) and phase reconstructions (right). (iii) Fluorescence data (left) and reconstructions (right). See also Videos 4 and 5.

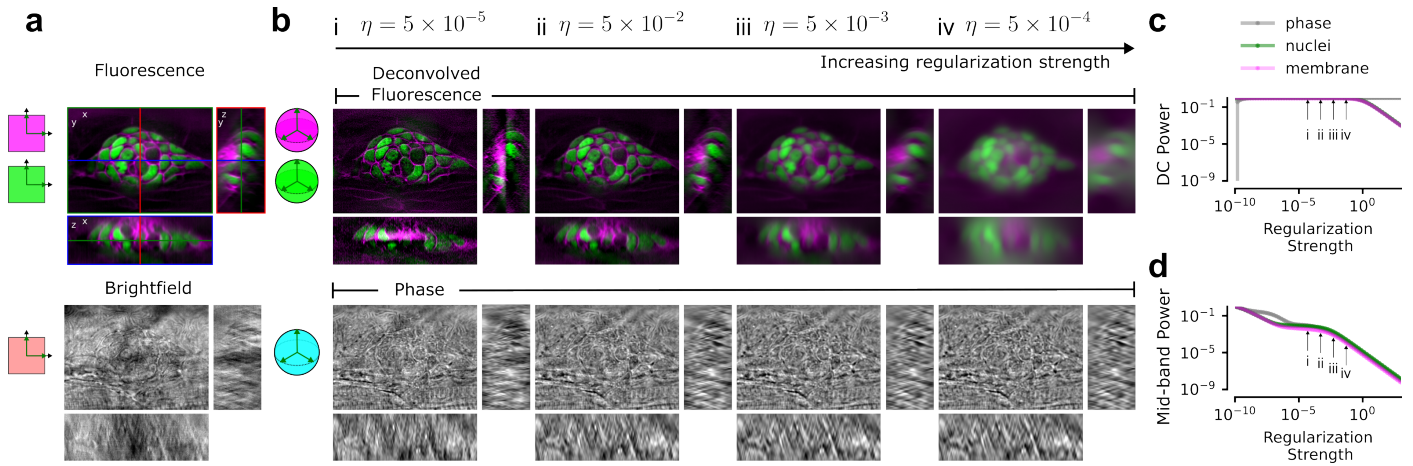


Fig. 5. Effect of regularization parameter on reconstructions. (a) Zebrafish neuromasts imaged in fluorescence and brightfield channels are (b) reconstructed over a range of regularization parameters, with small parameters generating noisy results and large parameters generating blurred results. Near the empirically selected optimal reconstruction (b, ii), the DC power (c) is nearly constant. In contrast, the mid-band power (d), the power for transverse spatial frequencies between one-eighth and one-quarter of the cutoff, changes when the regularization parameter is too high or too low and plateaus when the regularization parameter is in the correct range.

- I. E. Ivanov, E. Hirata-Miyasaki, T. Chandler, *et al.*, "Mantis: High-throughput 4D imaging and analysis of the molecular and physical architecture of cells," *PNAS Nexus* **3**, 323 (2024).
- S.-M. Guo, L.-H. Yeh, J. Folkesson, *et al.*, "Revealing architectural order with quantitative label-free imaging and deep learning," *eLife* **9**, e55502 (2020).
- E. Gómez-de Mariscal, M. Del Rosario, J. W. Pylvänäinen, *et al.*, "Harnessing artificial intelligence to reduce phototoxicity in live imaging," *J. Cell Sci.* **137**, jcs261545 (2024).
- Z. Liu, E. Hirata-Miyasaki, S. Pradeep, *et al.*, "Robust virtual staining of landmark organelles," (2024).
- B. Yang, M. Lange, A. Millett-Sikking, *et al.*, "DaXi—high-resolution, large imaging volume and multi-view single-objective light-sheet microscopy," *Nat. Methods* **19**, 461–469 (2022). Publisher: Nature Publishing Group.
- E. Sapoznik, B.-J. Chang, J. Huh, *et al.*, "A versatile oblique plane microscope for large-scale and high-resolution imaging of subcellular dynamics," *eLife* **9**, e57681 (2020). Publisher: eLife Sciences Publications, Ltd.
- K. H. Chen, A. N. Boettiger, J. R. Moffitt, *et al.*, "Spatially resolved, highly multiplexed RNA profiling in single cells," *Science* **348**, aaa6090 (2015). Publisher: American Association for the Advancement of Science.
- S. Black, D. Phillips, J. W. Hickey, *et al.*, "CODEX multiplexed tissue imaging with DNA-conjugated antibodies," *Nat. Protoc.* **16**, 3802–3835 (2021). Publisher: Nature Publishing Group.
- T. Kudo, A. M. Meireles, R. Moncada, *et al.*, "Multiplexed, image-based pooled screens in primary cells and tissues with PerturbView," *Nat. Biotechnol.* pp. 1–10 (2024). Publisher: Nature Publishing Group.
- D. Serwas and K. M. Davies, "Getting Started with In Situ Cryo-Electron Tomography," in *Cryo-EM: Methods and Protocols*, T. Gonen and B. L. Nannenga, eds. (Springer US, New York, NY, 2021), pp. 3–23.
- J. A. Pierson, J. E. Yang, and E. R. Wright, "Recent advances in correlative cryo-light and electron microscopy," *Curr. Opin. Struct. Biol.* **89**, 102934 (2024).
- A. S. Backer and W. E. Moerner, "Extending Single-Molecule Microscopy Using Optical Fourier Processing," *The J. Phys. Chem. B* **118**, 8313–8329 (2014).
- T. Chandler, H. Shroff, R. Oldenbourg, and P. La Rivière, "Spatio-angular fluorescence microscopy I Basic theory," *J. Opt. Soc. Am. A* **36**, 1334 (2019).
- N. Streibl, "Three-dimensional imaging by a microscope," *J. Opt. Soc. Am. A* **2**, 121 (1985).
- Y. Bao and T. K. Gaylord, "Quantitative phase imaging method based on an analytical nonparaxial partially coherent phase optical transfer function," *J. Opt. Soc. Am. A* **33**, 2125 (2016).
- P. Török, "Imaging of small birefringent objects by polarised light conventional and confocal microscopes," *Opt. Commun.* **181**, 7–18 (2000).
- R. Oldenbourg and P. Török, "Point-spread functions of a polarizing microscope equipped with high-numerical-aperture lenses," *Appl. Opt.* **39**, 6325 (2000).
- A. Saba, J. Lim, A. B. Ayoub, *et al.*, "Polarization-sensitive optical diffraction tomography," *Optica* **8**, 402–408 (2021). Publisher: Optical Society of America.
- S. Shin, J. Eun, S. S. Lee, *et al.*, "Tomographic measurement of dielectric tensors at optical frequency," *Nat. Mater.* **21**, 317–324 (2022). Number: 3 Publisher: Nature Publishing Group.
- L.-H. Yeh, I. E. Ivanov, T. Chandler, *et al.*, "Permittivity tensor imaging: modular label-free imaging of 3D dry mass and 3D orientation at high resolution," *Nat. Methods* pp. 1–18 (2024). Publisher: Nature Publishing Group.
- O. Zhang, Z. Guo, Y. He, *et al.*, "Six-dimensional single-molecule imaging with isotropic resolution using a multi-view reflector microscope," *Nat. Photonics* **17**, 179–186 (2023).
- T. Chandler, M. Guo, Y. Su, *et al.*, "Three-dimensional spatio-angular fluorescence microscopy with a polarized dual-view inverted selective-plane illumination microscope (pol-diSPIM)," (2024).
- H. H. Hopkins, "The concept of partial coherence in optics," *Proc. Royal Soc. London. Ser. A. Math. Phys. Sci.* **208**, 263–277 (1951).
- H. H. Barrett and K. J. Myers, *Foundations of image science*, Wiley series in pure and applied optics (Wiley-Interscience, Hoboken, NJ, 2004).
- S. B. Mehta and C. J. R. Sheppard, "Partially coherent microscope in phase space," *J. Opt. Soc. Am. A* **35**, 1272 (2018).
- C. J. R. Sheppard, "Partially coherent microscope imaging system in phase space: effect of defocus and phase reconstruction," *J. Opt. Soc. Am. A* **35**, 1846 (2018).
- E. Wolf, *Introduction to the theory of coherence and polarization of light* (Cambridge Univ. Press, Cambridge, 2007), 1st ed.
- M. A. Bruce and M. J. Butte, "Real-time GPU-based 3D Deconvolution," *Opt. Express* **21**, 4766 (2013).
- E. Wernersson, E. Gelali, G. Girelli, *et al.*, "Deconvolf enables high-performance deconvolution of widefield fluorescence microscopy im-

- ages," *Nat. Methods* **21**, 1245–1256 (2024).
31. K. Herath, U. Haputhanthri, R. Hettiarachchi, *et al.*, "Differentiable Microscopy Designs an All Optical Phase Retrieval Microscope," (2022).
 32. D. Deb, G.-J. Both, A. Chaware, *et al.*, "Chromatix: a high-performance differentiable wave optics simulation library," in *Computational Optics 2024*, D. G. Smith and A. Erdmann, eds. (SPIE, Strasbourg, France, 2024), p. 45.
 33. O. Zhang and M. D. Lew, "Single-molecule orientation localization microscopy I: fundamental limits," *J. Opt. Soc. Am. A* **38**, 277 (2021).
 34. P. C. Hansen, "The L-curve and its use in the numerical treatment of inverse problems," (2005).
 35. T. H. Edwards and S. Stoll, "Optimal Tikhonov regularization for DEER spectroscopy," *J. Magn. Reson.* **288**, 58–68 (2018).
 36. S. B. Mehta, M. Shribak, and R. Oldenbourg, "Polarized light imaging of birefringence and diattenuation at high resolution and high sensitivity," *J. Opt.* **15**, 094007 (2013).
 37. M. Sakakura, Y. Lei, L. Wang, *et al.*, "Ultralow-loss geometric phase and polarization shaping by ultrafast laser writing in silica glass," *Light. Sci. & Appl.* **9**, 15 (2020).
 38. A. Villani, J. Benjaminsen, C. Moritz, *et al.*, "Clearance by Microglia Depends on Packaging of Phagosomes into a Unique Cellular Compartment," *Dev. Cell* **49**, 77–88.e7 (2019).
 39. N. Ortega-Quijano and J. L. Arce-Diego, "Generalized Jones matrices for anisotropic media," *Opt. Express* **21**, 6895 (2013).
 40. F. G. Ledesma and M. Mewes, "Spherical-harmonic tensors," *Phys. Rev. Res.* **2**, 043061 (2020).
 41. M. Gell-Mann, "Symmetries of Baryons and Mesons," *Phys. Rev.* **125**, 1067–1084 (1962).
 42. J. J. Gil and R. Ossikovski, *Polarized Light and the Mueller Matrix Approach* (CRC Press, Boca Raton, 2017), 1st ed.
 43. M. R. Arnison and C. J. Sheppard, "A 3D vectorial optical transfer function suitable for arbitrary pupil functions," *Opt. Commun.* **211**, 53–63 (2002).
 44. J. T. Fourkas, "Rapid determination of the three-dimensional orientation of single molecules," *Opt. Lett.* **26**, 211 (2001).
 45. D. J. Griffiths, *Introduction to electrodynamics* (Cambridge university press, Cambridge, 2017), 4th ed.
 46. C. J. R. Sheppard, S. S. Kou, and J. Lin, "The Green-function transform and wave propagation," *Front. Phys.* **2** (2014).
 47. T. Noda, S. Kawata, and S. Minami, "Three-dimensional phase contrast imaging by an annular illumination microscope," *Appl. Opt.* **29**, 3810 (1990).
 48. R. A. Claus, P. P. Naulleau, A. R. Neureuther, and L. Waller, "Quantitative phase retrieval with arbitrary pupil and illumination," *Opt. Express* **23**, 26672 (2015).

10. SUPPLEMENT: TABLE OF NOTATIONS

symbol	description
\mathbf{b}	background data
$b_c^{(m)}$	background data by channel & contrast mode
\mathbf{d}	data channels
$d_c^{(m)}(\mathbf{r}_d)$	volume of data for a channel & contrast mode
$D_c^{(m)}(\mathbf{v})$	data spectrum for a channel & contrast mode
$\delta(\mathbf{v})$	delta function
$\mathbf{e}^{(d)}$	direct fields
\mathbf{f}	material properties
$f_p^{(m)}(\mathbf{r}_o)$	material property volume by contrast mode
$F_p^{(m)}(\mathbf{v})$	material properties spectrum by contrast mode
$f_{ij}^{(lf)}$	permittivity tensor
$f_i^{(fl)}$	fluorescence dipole moment
(fl)	fluorescence
$g_{ij}(\mathbf{r})$	Green's tensor
$G_{ij}(\mathbf{v})$	Green's tensor spectrum
\mathcal{H}	imaging forward operator
$h_{cp}^{(m)}(\mathbf{r})$	point-spread function by channel, material property, and contrast mode
$H_{cp}^{(m)}(\mathbf{v})$	transfer function by channel, material property, and contrast mode
η	regularization parameter
(lf)	label free
$P_{ij}(\mathbf{v})$	tensor detection pupil
ρ	density
Q	scalar objective function
\mathcal{R}	reconstruction operator
\mathbf{r}_d	3D data-space coordinate
\mathbf{r}_o	3D object-space coordinate
(tls)	Tikhonov least squares
\mathcal{S}	scattering operator
$S_i(\mathbf{v})$	vector source pupil
\mathbf{v}	3D spatial frequency coordinate
\mathcal{V}	virtual staining operator
\dagger	conjugate transpose

11. SUPPLEMENT: IMAGING EXPERIMENTS

A. Spoke target

We imaged a femtosecond laser-written anisotropic glass target with spoke patterns containing a radial transverse birefringent pattern. Fabrication is described in detail elsewhere [21, 37].

The target was imaged with label-free contrast using circularly polarized light and four elliptically polarized states with swing of 0.1 waves as described in [3]. The sample was illuminated with 450 nm light with a $NA_{\text{ill}} = 0.52$ condenser, a $NA_{\text{det}} = 1.35$ objective, a Prime-BSI sCMOS with 6.5 μm pixels, and remote-refocus axial steps spaced by 0.25 μm in sample space.

B. A549 cells

A549 cells were endogenously tagged with fluorescent proteins and imaged as described in [2]. Briefly, cells were plated and imaged simultaneously in label-free and fluorescent contrast modes. Label-free contrast was generated by illuminating the sample using a $NA_{\text{ill}} = 0.52$ condenser and 450 nm light with one circular and four elliptical polarization states with swing

of 0.05 waves as described in [3]. Transmitted light was collected using a $NA_{\text{det}} = 1.35$ objective, analyzed with a circular analyzer of opposite handedness, and imaged on a Prime-BSI sCMOS camera with 6.5 μm pixels. Axial scanning with 0.225 μm steps was achieved with a remote-refocus system. Fluorescence contrast was measured in two channels in a single-objective light-sheet configuration.

C. Zebrafish

Zebrafish were raised at the Cardiovascular Research Institute (CVRI) at UCSF by following standard protocols in accordance with IACUC, UCSF. Casper zebrafish bearing the Tg(mpeg1.1:EGFP-CAAX) transgene [38] were raised to 8dpf for imaging for imaging. Larvae were anesthetized by placing in 0.02% solution of MS222 (Tricaine) in embryo medium. The anesthetized larvae were mounted in 1% agarose in a 4-well aluminum imaging chamber with Ibidi polymer coverslips to promote oxygen exchange. 0.02% MS222 solution was poured on the agarose for hydration. The imaging chamber was maintained at 28° during the course of the experiment.

Larvae were imaged with label-free contrast under 532 nm light with a $NA_{\text{ill}} = 0.45$ condenser and a 20 \times , $NA_{\text{det}} = 0.55$ objective and a Prime-BSI sCMOS with 6.5 μm pixels and 2 μm stage-motion axial steps. Five polarized states were collected with swing of 0.1 waves. Fluorescence contrast was generated with ~ 450 nm illumination and a 516 nm-centered FITC filter set. Eleven fields of view were imaged sequentially to image the entire fish. Raw data were background corrected and reconstructed. The overlapping regions of each FOV were registered by minimizing the phase cross-correlation, and the registered images were stitched with linear blending in the overlapping regions.

Following imaging, larvae were euthanized through hypothermic shock.

D. Zebrafish neuromasts

This study uses transgenic zebrafish lines expressing she:H2B-EGFP and cldnb:lyn-mScarlet to label the nucleus and the cell membrane of the neuromasts, respectively. The zebrafish were handled with an approved IACUC protocol by Tiger Lao and imaged at 3dpf (days post-fertilization: dpf). This dataset is part of the test dataset used in virtual staining [5]. The neuromast was acquired with brightfield and two fluorescence channels using 0.52 NA condenser, Nikon PlanApo VC x63 1.2NA objective on an ASI Rapid Automated Modular Microscope System (RAMM) through the same optical path using a Andor ZYLA-4.2P-USB3-W-2V4 sCMOS camera.

12. SUPPLEMENT: NOTATION AND CONVENTIONS

We adopt Einstein notation throughout the supplements. If an index does not appear on both sides of the equation, then a sum or integral over that index is implied. For example, matrix multiplication can be written without explicitly writing the sum

$$y_i = \sum_j A_{ij}x_j \longleftrightarrow y_i = A_{ij}x_j, \quad (10)$$

and convolution can be written without explicitly writing the integral

$$g(r) = \int_{\mathbb{R}} dr' h(r-r')f(r') \longleftrightarrow g(r) = h(r-r')f(r'). \quad (11)$$

We use boldface for vectors (e.g. \mathbf{r} , \mathbf{v} , $\boldsymbol{\tau}$). We use \mathbf{r} for position vectors, and we use \mathbf{v} and $\boldsymbol{\tau}$ for spatial frequency vectors. We use capital letters to denote Fourier transforms. For example

$$F(\mathbf{v}) = f(\mathbf{r}) \exp[i2\pi\mathbf{r} \cdot \mathbf{v}], \quad (12)$$

where the integral on the right-hand side is implied.

13. SUPPLEMENT: CONTRAST-SEPARABLE IMAGING SYSTEMS

In many microscopy imaging systems, data in each channel is the sum of the contributions from each material property. We call these systems *channel linear* and we can express the forward operator as

$$\mathbf{d}_c = \mathcal{H}_{cp} \mathbf{f}_p + \mathbf{b}_c \quad (13)$$

where c indexes channels and p indexes material properties. For example, multi-channel fluorescence microscopy often suffers from crosstalk, but these systems are still channel linear if the data is the sum of the contribution from each type of fluorophore.

When there is no crosstalk between channels (for example, when fluorescence filters are perfect), we say the imaging system is *channel separable*, which implies that the system can be written as

$$\mathbf{d}_c = \mathcal{H}_{cc} \mathbf{f}_c + \mathbf{b}_c, \quad (14)$$

i.e. the operator \mathcal{H} is *diagonal over channels*.

The waveOrder framework considers imaging systems where some groups of channels are separable (e.g. fluorescence contrast), and some groups of channels are merely linear (e.g. label-free contrast). We call such imaging systems *contrast separable* and they can be expressed as

$$\mathbf{d}_c^{(m)} = \mathcal{H}_{cp}^{(m)} \mathbf{f}_p^{(m)} + \mathbf{b}_c^{(m)}, \quad (15)$$

where m indexes each of the M *contrast modes*. For example, an imaging system with two channel-separable fluorescent channels and four channel-linear label-free data channels that jointly encode three object properties can be written as

$$\begin{bmatrix} \mathbf{d}_1^{(1)} \\ \mathbf{d}_1^{(2)} \\ \mathbf{d}_1^{(3)} \\ \mathbf{d}_2^{(3)} \\ \mathbf{d}_2^{(3)} \\ \mathbf{d}_2^{(3)} \end{bmatrix} = \begin{bmatrix} \mathcal{H}_{1,1}^{(1)} & 0 & 0 & 0 & 0 \\ 0 & \mathcal{H}_{1,1}^{(2)} & 0 & 0 & 0 \\ 0 & 0 & \mathcal{H}_{1,1}^{(3)} & \mathcal{H}_{1,2}^{(3)} & \mathcal{H}_{1,3}^{(3)} \\ 0 & 0 & \mathcal{H}_{2,1}^{(3)} & \mathcal{H}_{2,2}^{(3)} & \mathcal{H}_{2,3}^{(3)} \\ 0 & 0 & \mathcal{H}_{3,1}^{(3)} & \mathcal{H}_{3,2}^{(3)} & \mathcal{H}_{3,3}^{(3)} \\ 0 & 0 & \mathcal{H}_{4,1}^{(3)} & \mathcal{H}_{4,2}^{(3)} & \mathcal{H}_{4,3}^{(3)} \end{bmatrix} \begin{bmatrix} \mathbf{f}_1^{(1)} \\ \mathbf{f}_1^{(2)} \\ \mathbf{f}_1^{(3)} \\ \mathbf{f}_2^{(3)} \\ \mathbf{f}_3^{(3)} \end{bmatrix} + \begin{bmatrix} \mathbf{b}_1^{(1)} \\ \mathbf{b}_1^{(2)} \\ \mathbf{b}_1^{(3)} \\ \mathbf{b}_2^{(3)} \\ \mathbf{b}_2^{(3)} \\ \mathbf{b}_2^{(3)} \end{bmatrix}. \quad (16)$$

In other words, we assume that the forward operator is *block diagonal over channels*, so we can split our reconstruction problem into subproblems, one for each contrast mode

$$\hat{\mathbf{f}}_p^{(m)} = \mathcal{R}_\eta^{(m)} \mathbf{d}_c^{(m)} = \underset{\mathbf{f}_p^{(m)}}{\operatorname{argmin}} Q_\eta^{(\text{tls})}(\mathbf{f}_p^{(m)}, \mathbf{d}_c^{(m)}), \quad (17)$$

where we have defined $\mathcal{R}_\eta^{(m)}$ as a *reconstruction operator* for each contrast mode. Equation 17 is the core of our reconstruction algorithm.

14. SUPPLEMENT: RECONSTRUCTION ALGORITHM

For each contrast mode, the forward operators in Equation 15 can be decomposed using the singular value decomposition

$$\mathcal{H} = \sum_i^R \sigma_i \mathbf{u}_i \mathbf{v}_i^\dagger, \quad (18)$$

where R is the rank of \mathcal{H} , $\{\mathbf{u}_i\}$ is a set of orthonormal data-space vectors that span the space of deterministic expected data, and $\{\mathbf{v}_i\}$ is a set of orthonormal object-space vectors that span the measurement space of object properties.

We use this decomposition to solve Equation 17 in a single step for each mode

$$\mathcal{R}_\eta = \sum_i^R \frac{\sigma_i}{\sigma_i^2 + \eta} \mathbf{v}_i \mathbf{u}_i^\dagger. \quad (19)$$

In practice we choose a different regularization parameter η for each contrast mode. Supplement Figure 6 demonstrates a multi-channel reconstruction through a regularization sweep.

15. SUPPLEMENT: MODEL OF SPECIMEN PROPERTIES

Following earlier work [21], we model elastic light-matter interactions with a 3D spatial distribution of relative permittivity tensors $\epsilon_{ij}^{(r)}(\mathbf{r}_o)$, where \mathbf{r}_o is a 3D spatial position vector, i and j are the indices of the rank-2 tensor, and (r) is short for relative to indicate that the permittivity tensor is relative to the permittivity of vacuum and therefore unitless. The permittivity tensor is the relationship between an incident electric field e_j and the dipole moment p_i it induces in the material

$$p_i = \epsilon_{ij}^{(r)} e_j. \quad (20)$$

The elements $\epsilon_{ij}^{(r)}$ are complex, accounting for both the amplitude and phase of the induced dipole moments.

We assume that the spatial distribution of relative permittivity tensors is dominated by a spatially uniform and angularly isotropic *relative permittivity of the medium*, $\epsilon^{(\text{rm})}$. Subtracting the medium's contribution and changing units to match convention results in the our main object of interest, the *scattering potential tensor*

$$f_{ij}^{(\text{lf})}(\mathbf{r}_o) = k_0^2 (\epsilon_{ij}^{(r)}(\mathbf{r}_o) - \epsilon^{(\text{rm})} \delta_{ij}), \quad (21)$$

where $k_0 = 2\pi/\lambda_0$ is the free-space wave number, and λ_0 is the free-space wavelength. The scattering potential tensor can be interpreted as the relationship between the incident electric field and the induced dipole moment *above background* in media with an isotropic background.

If the scattering potential tensor $f_{ij}(\mathbf{r}_o)$ is small compared to the isotropic background $k_0^2 \epsilon^{(\text{rm})} \delta_{ij}$, we can approximate the scattering potential tensor by expanding it in terms of a basis

$$f_{ij}^{(\text{lf})}(\mathbf{r}_o) \approx \mathbf{f}_{\ell m}^{(\text{lf})}(\mathbf{r}_o) \mathcal{Y}_{\ell m}^{ij}, \quad \ell \in \{0, 1, 2\}, \quad -\ell \leq m \leq \ell, \quad (22)$$

where $\mathbf{f}_{\ell m}(\mathbf{r}_o)$ are expansion coefficients and $\mathcal{Y}_{\ell m}^{ij}$ are basis vectors

$$\begin{aligned} \mathcal{Y}_{00} &= \frac{1}{\sqrt{3}} \begin{bmatrix} 1 & 0 & 0 \\ 0 & 1 & 0 \\ 0 & 0 & 1 \end{bmatrix}, \mathcal{Y}_{1,-1} = \frac{1}{\sqrt{2}} \begin{bmatrix} 0 & 0 & -1 \\ 0 & 0 & 0 \\ 1 & 0 & 0 \end{bmatrix}, \mathcal{Y}_{1,1} = \frac{1}{\sqrt{2}} \begin{bmatrix} 0 & -1 & 0 \\ 0 & 0 & 0 \\ 0 & 0 & 0 \end{bmatrix}, \\ \mathcal{Y}_{1,0} &= \frac{1}{\sqrt{2}} \begin{bmatrix} 0 & 0 & 0 \\ 0 & 0 & -1 \\ 0 & 1 & 0 \end{bmatrix}, \mathcal{Y}_{2,-2} = \frac{1}{\sqrt{2}} \begin{bmatrix} 1 & 0 & 0 \\ 0 & -1 & 0 \\ 0 & 0 & 0 \end{bmatrix}, \mathcal{Y}_{2,-1} = \frac{1}{\sqrt{2}} \begin{bmatrix} 0 & 0 & 0 \\ 0 & 0 & 1 \\ 0 & 1 & 0 \end{bmatrix}, \\ \mathcal{Y}_{2,0} &= \frac{1}{\sqrt{6}} \begin{bmatrix} -1 & 0 & 0 \\ 0 & -1 & 0 \\ 0 & 0 & 2 \end{bmatrix}, \mathcal{Y}_{2,1} = \frac{1}{\sqrt{2}} \begin{bmatrix} 0 & 0 & 1 \\ 0 & 0 & 0 \\ 1 & 0 & 0 \end{bmatrix}, \mathcal{Y}_{2,2} = \frac{1}{\sqrt{2}} \begin{bmatrix} 1 & 0 & 0 \\ 0 & -1 & 0 \\ 0 & 0 & 0 \end{bmatrix}. \end{aligned} \quad (23)$$

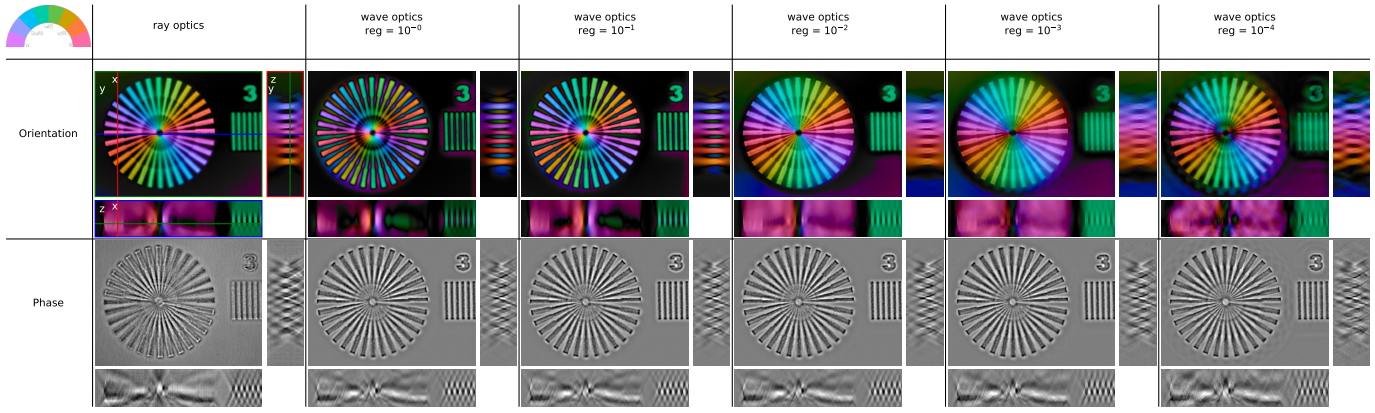


Fig. 6. Top row: Orientation and transverse birefringence. **Bottom row:** Brightfield and phase. **First column:** Ray optics reconstruction of orientation with raw brightfield data. **Subsequent columns:** Wave optical reconstruction of transverse birefringence and phase with increasing regularization parameter.

Notice the approximation—the scattering potential tensors $f_{ij}^{(fl)}$ are members of $GL(3, \mathbb{C})$, the group of complex 3×3 matrices, so they cannot be expanded into a sum because they do not form a vector space. We can approximate the scattering potential tensors by expanding them into $gl(3, \mathbb{C})$, the Lie algebra of $GL(3, \mathbb{C})$, which forms a vector space near the identity.

The vectors $\mathcal{Y}_{\ell m}^{ij}$ form an orthonormal basis for $gl(3, \mathbb{C})$, and their 18 coefficients (9 real, 9 imaginary) enable clear physical interpretations:

- $\text{Re}(f_{\ell m})$ are phase and birefringence components,
- $\text{Im}(f_{\ell m})$ are absorption and diattenuation components,
- $f_{0,m}$ are isotropic absorption and phase components,
- $f_{1,m}$ are circular diattenuation and birefringence components,
- $f_{2,m}$ are linear diattenuation and birefringence components, and
- $f_{2,\pm 2}$ are transverse linear diattenuation and birefringence components.

We note that here we use the index tuple (ℓ, m) to indicate the row and column of the spherical harmonic tensor as shown in Figure 1. In the main text, we reduce this index tuple to a single index with $p = \ell(\ell + 1) + m$.

Near variants of the basis $\mathcal{Y}_{\ell m}^{ij}$ appear in the literature as differential Jones matrices [39], spherical harmonic tensors [40], and the Gell-Mann matrices [41].

Fluorescence contrast is generated by the second dipole moments $\langle f_i^{(fl)}(\mathbf{r}_o) f_j^{(fl)}(\mathbf{r}_o) \rangle$, which can also be expanded onto the spherical harmonic tensors as

$$\langle f_i^{(fl)}(\mathbf{r}_o) f_j^{(fl)}(\mathbf{r}_o) \rangle = f_c^{(fl)}(\mathbf{r}_o) \mathcal{Y}_{\ell m}^{ij}. \quad (24)$$

16. SUPPLEMENT: MODEL OF MEASURABLE DATA

We measure the Stokes parameters throughout three-dimensional volumes by assembling polarization-resolved 2D

images into a 3D defocus stack. We denote this dataset with $d_c(\mathbf{r}_d)$ where $c \in \{0, 1, 2, 3\}$ and \mathbf{r}_d is a 3D detector coordinate.

In addition to the Stokes parameters, we find an intermediate representation called the *coherency matrix* to be a convenient way to manage our data and models. We briefly review the relationship between the Stokes parameters and the coherency matrix below.

Consider a stochastic two-component electric field e_i ($i \in x, y$) incident on a detector. The stochasticity might arise from randomness in the source or from multiple individually coherent but mutually incoherent beams being combined together.

We can model all of the second-order observables (for example, from observing the intensity behind a variable polarizer) from these fields by forming the coherency matrix (or *polarization matrix*) as the time-averaged conjugate outer product of the fields

$$\phi_{i'i'} = \langle e_i e_{i'}^* \rangle. \quad (25)$$

Clearly, $\phi_{i'i'} = \phi_{i'i'}^*$, so the diagonal elements are real and the off-diagonal elements form a conjugate pair. Additionally, $\phi_{i'i'}$ is a positive semi-definite matrix, so its trace and determinant are real and non-negative.

The coherency matrix can be expanded into a more interpretable form using the Pauli matrices, $\sigma_n^{i'i'}$, explicitly

$$\begin{aligned} \sigma_0 &= \begin{bmatrix} 1 & 0 \\ 0 & 1 \end{bmatrix}, & \sigma_1 &= \begin{bmatrix} 1 & 0 \\ 0 & -1 \end{bmatrix}, \\ \sigma_2 &= \begin{bmatrix} 0 & 1 \\ 1 & 0 \end{bmatrix}, & \sigma_3 &= \begin{bmatrix} 0 & -i \\ i & 0 \end{bmatrix}. \end{aligned} \quad (26)$$

The Stokes parameters are real-valued observables given by

$$d_c = \sigma_c^{i'i'} \phi_{i'i'}. \quad (27)$$

Notice that this is an element-wise dot product, not a matrix multiplication. Expanding Eqs. 25–27 results in the familiar formulas

$$\begin{aligned} d_0 &= \langle e_x e_x^* \rangle + \langle e_y e_y^* \rangle, & d_1 &= \langle e_x e_x^* \rangle - \langle e_y e_y^* \rangle, \\ d_2 &= \langle e_x e_y^* \rangle + \langle e_y e_x^* \rangle, & d_3 &= -i \langle e_x e_y^* \rangle + i \langle e_y e_x^* \rangle. \end{aligned} \quad (28)$$

The non-negative trace of $\phi_{i'i'}$ corresponds to the constraint $d_0 \geq 0$ (the intensity of the beam is positive), and the non-negative

determinant of $\phi_{ii'}$ corresponds to the constraint $d_0^2 \geq d_1^2 + d_2^2 + d_3^2$ (the degree of polarization does not exceed one) [42].

17. SUPPLEMENT: IMAGING MODEL

In this section we find linear relationships between the Stokes volumes, $d_c(\mathbf{r}_d)$, and the main objects of our model: the scattering tensor expansion coefficients $f_{\ell m}^{(\text{lf})}(\mathbf{r}_o)$ and the second moments matrix expansion coefficients $f_{\ell m}^{(\text{f})}(\mathbf{r}_o)$.

We start by describing three key elements of our model—our illumination model, our scattering model, and our detection model. We then combine these elements into a complete forward model, where contrast is generated by interference. Finally, we compute contrast transfer functions, and we show that that these transfer functions can be efficiently computed with 3D correlations of Ewald caps.

A. Illumination model

We consider illumination from a perfectly polarized, quasi-monochromatic, spatially incoherent source imaged into the back aperture of a high numerical aperture condenser (Köhler illumination). The source is spatially incoherent, so the fields that are generated by each point on the source do not interfere until they reach the detector. Therefore, for intermediate planes we need to keep track of the fields created by each incoherent point of the source.

We model the fields in the sample space $e_k^{(i)}$ at point \mathbf{r}_o due to a source point at $\boldsymbol{\tau}$ as a weighted plane wave

$$e_k^{(i)}(\mathbf{r}'_o, \boldsymbol{\tau}) = S_k(\boldsymbol{\tau}) \exp(i2\pi \mathbf{r}'_o \cdot \boldsymbol{\tau}), \quad (29)$$

where $S_k(\boldsymbol{\tau})$ is our *vector source pupil*. Although $\boldsymbol{\tau}$ is a spatial-frequency coordinate, it can be interpreted as an renormalized spatial coordinate due to the Fourier-transform relationship between the sample space and the back aperture space.

Our source pupil $S_k(\boldsymbol{\tau})$ is the core of our illumination model, and we model it as a uniformly polarized pupil

$$S_k(\boldsymbol{\tau}) = e_k^{(s)} S(\boldsymbol{\tau}), \quad (30)$$

where $e_k^{(s)}$ is a two-component Jones vector (we ignore axial components), and $S(\boldsymbol{\tau})$ is a scalar source pupil, which can be expressed as an Ewald cap

$$S(\boldsymbol{\tau}) = \text{Ew}(\boldsymbol{\tau}, \text{NA}_{\text{ill}}/\lambda), \quad (31)$$

with

$$\text{Ew}(\boldsymbol{\tau}, \tau_c) = \frac{\Delta\tau}{\sqrt{\lambda\tau_{\parallel}}} \delta\left(\tau_{\parallel} - \sqrt{\lambda^{-2} - |\boldsymbol{\tau}_{\perp}|^2}\right) \text{rect}\left(\frac{|\boldsymbol{\tau}_{\perp}|}{\tau_c}\right), \quad (32)$$

where NA_{ill} is the illumination numerical aperture, $\boldsymbol{\tau}_{\perp}$ is the transverse spatial frequency, τ_{\parallel} is the axial spatial frequency, $\Delta\tau$ is the bandwidth of the quasi-monochromatic light, τ_c is the cutoff frequency, and $\text{rect}(x) = 1$ for $|x| < 1/2$ and 0 elsewhere. The Ew function's rect term cuts off the transmitted frequencies at the numerical aperture, the δ term specifies a hemispherical shell to model the quasi-monochromatic illumination, the $1/\sqrt{\lambda\tau_{\parallel}}$ term is an apodization term that upweights marginal spatial frequencies to preserve power and Abbe's sine condition [43], and the $\Delta\tau$ term keeps the Ewald cap unitless.

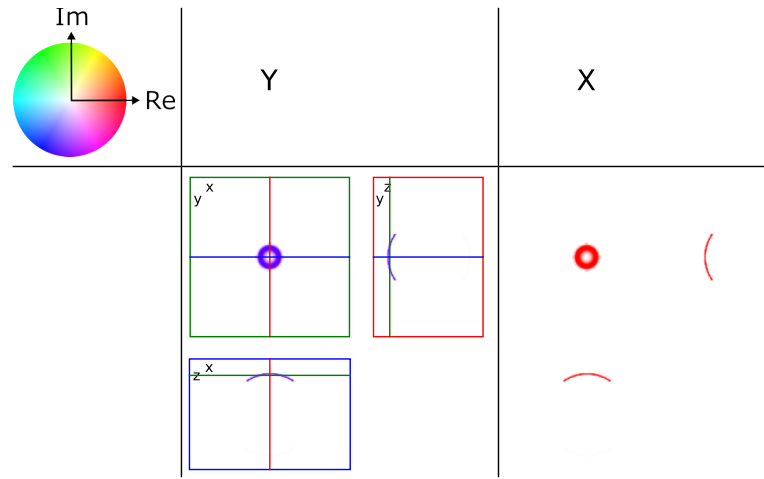


Fig. 7. Vector source pupil $S_k(\boldsymbol{\tau})$ with $\text{NA}_{\text{ill}} = 0.5$ illuminated with circularly polarized light ($e_x^{(s)} = 1$ and $e_y^{(s)} = -i$).

More sophisticated models may include axial illumination components, vector aberrations, or vector masks by modifying the vector source pupil $S_k(\boldsymbol{\tau})$.

The Ewald sphere is challenging to sample directly because it is a thin shell. Instead we simulate its axial Fourier transform and take its numerical inverse axial Fourier transform

$$\text{Ew}(\boldsymbol{\tau}, \tau_c) = \frac{\Delta\tau}{\sqrt{\lambda\tau_{\parallel}}} \mathcal{F}_{\parallel}^{-1} \left\{ \exp \left[i2\pi r_{\parallel} \sqrt{\lambda^{-2} - |\boldsymbol{\tau}_{\perp}|^2} \right] \right\} \text{rect} \left(\frac{|\boldsymbol{\tau}_{\perp}|}{\tau_c} \right). \quad (33)$$

Figure 7 shows sections through our numerical model for the vector source pupil.

B. Scattering model

The scalar Green's function is the impulse response of the scalar Helmholtz operator—the field created by an isotropic point emitter. The far-field scalar Green's function takes the form of a spherical wave

$$g(\mathbf{r}) = \frac{\exp(i2\pi|\mathbf{r}|/\lambda)}{4\pi|\mathbf{r}|}, \quad (34)$$

where \mathbf{r} is a 3D position vector and λ is the wavelength in the medium.

The Green's tensor is the impulse response of the vector Helmholtz operator—the vector fields created by a point dipole emitter. Dipole emitters can be linear, circular, or elliptical, and they can have any 3D orientation. Therefore, we need to represent a dipole emitter with a complex-valued vector \mathbf{p} . For example $\mathbf{p} = [1, i, 0]^T / \sqrt{2}$ represents a unit circular dipole in the x - y plane.

To find the 3D vector fields created by an arbitrary 3D dipole emitter, we need a 3×3 tensor $g_{ij}(\mathbf{r})$, which takes the form

$$g_{ij}(\mathbf{r}) = (\delta_{ij} - r_i r_j) g(\mathbf{r}), \quad (35)$$

where δ_{ij} is the Kronecker delta and r_i are the components of \mathbf{r} . The vector fields created in the far field $e_i(\mathbf{r})$ can be found by matrix multiplication of the Green's tensor and the dipole emitter $e_i(\mathbf{r}) = g_{ij}(\mathbf{r}) p_j$.

Some readers will be familiar with expressions of the form $\mathbf{e} \propto \mathbf{r} \times \mathbf{p} \times \mathbf{r}$ for finding far-field dipole emission patterns [44, 45]. This formulation is identical to the Green's tensor formulation because $\hat{\mathbf{r}} \times \hat{\mathbf{p}} \times \hat{\mathbf{r}} = (I - \mathbf{r}\mathbf{r}^T)\mathbf{p}$, where I is the identity. While both forms are correct, the Green's tensor formulation is conveniently in matrix form, so it can be precomputed and easily applied to arbitrary dipole emitters.

The far-field Green's tensor spectrum $G_{ij}(\mathbf{v})$ is the 3D Fourier transform of the Green's tensor. Computing this Fourier transform symbolically is subtle, involving both on- and off-shell components [46], and results in

$$G_{ij}(\mathbf{v}) = \left[\delta_{ij} - \lambda^{-2} v_i v_j \right] \left[\frac{1}{\pi(|\mathbf{v}|^2 - \lambda^{-2})} + \frac{i}{2\lambda} \delta(|\mathbf{v}|^2 - \lambda^{-2}) \right]. \quad (36)$$

Sampling $G_{ij}(\mathbf{v})$ directly is challenging because it primarily consists of a thin shell. In this work we approximate the Green's tensor spectrum by sampling $g_{ij}(\mathbf{r})$ on a regular grid, take its 3D discrete Fourier transform, then ignore its real part. While the Green's tensor has a real off-shell component, this component is challenging to handle numerically and it is filtered to zero during downstream detection. Therefore, in Figure 8 we show a purely imaginary Green's tensor spectrum.

The Green's tensor has several properties that are useful for verifying correct implementations. First, the Green's tensor is rotationally invariant $g_{ij}(\mathbf{r}) = R_{ik} g_{kl}(\mathbf{r}) R_{j\ell}$ for all rotation matrices $R_{ik} \in \text{SO}(3)$. Physically, this means that rotating a dipole, computing its emitted fields, then rotating the fields back results in the same fields as computing the fields directly. Second, the Green's tensor creates purely polarized fields, so the emitted fields $e_i(\mathbf{r}) = g_{ij}(\mathbf{r}) p_j$ should have an outer product $e_i(\mathbf{r}) e_j(\mathbf{r})$ with zero determinant.

C. Detection model

We use a detection model that tracks how the 3D volumetric fields in sample space $e_k^{(o)}(\mathbf{r}_o, \boldsymbol{\tau})$ are mapped to 2D (transverse) volumetric fields on the detector $e_i^{(d)}(\mathbf{r}_d, \boldsymbol{\tau})$. We assume that our detection optics are shift invariant, and we write our model as

$$e_i^{(d)}(\mathbf{r}_d, \boldsymbol{\tau}) = p_{ij}(\mathbf{r}_d - \mathbf{r}_o) e_j^{(o)}(\mathbf{r}_o, \boldsymbol{\tau}), \quad (37)$$

where $p_{ij}(\mathbf{r}_d - \mathbf{r}_o)$ is the i th-component response due to the j th-component input, so p_{ij} is a 2×3 tensor.

We describe our detection model with its Fourier-space response

$$P_{ij}(\mathbf{v}) = \delta_{ij} \text{Ew}(\mathbf{v}, \text{NA}_{\text{det}}/\lambda), \quad (38)$$

where NA_{det} is the detection numerical aperture. We approximate the response of the detection objective with the δ_{ij} term, which effectively ignores the objectives's rotation effects— x/y -component inputs are transmitted to purely x/y -component outputs. Considering field rotation and aberrations are areas for future work.

D. Label-free forward model

The critical step is modeling how illuminating fields $e_k^{(i)}(\mathbf{r}'_o, \boldsymbol{\tau})$ interact with the sample $f_{nk}(\mathbf{r}'_o)$ to generate object-space fields $e_j^{(o)}(\mathbf{r}_o, \boldsymbol{\tau})$. If we consider only single-scattering events, the first-Born approximation, then

$$e_j^{(o)}(\mathbf{r}_o, \boldsymbol{\tau}) = \left[g_{jn}(\mathbf{r}_o - \mathbf{r}'_o) f_{nk}(\mathbf{r}'_o) + \delta_{jk} \delta(\mathbf{r}_o - \mathbf{r}'_o) \right] e_k^{(i)}(\mathbf{r}'_o, \boldsymbol{\tau}), \quad (39)$$

where the first term in square brackets represents scattered fields, the second term represents direct terms fields, and $g_{jn}(\mathbf{r}_o - \mathbf{r}'_o)$ is the Green's tensor. Notice that the sums over p and k and the integral over \mathbf{r}'_o are implied by Einstein notation.

Next, we find the fields incident on the 3D detector,

$$e_i^{(d)}(\mathbf{r}_d, \boldsymbol{\tau}) = p_{ij}(\mathbf{r}_d - \mathbf{r}_o) e_k^{(o)}(\mathbf{r}_o, \boldsymbol{\tau}) \quad (40)$$

Finally, we can calculate the observables on the detector by taking the outer product of the fields

$$\Phi_{ii'}^{(d)}(\mathbf{r}_d) = e_i^{(d)}(\mathbf{r}_d, \boldsymbol{\tau}) e_{i'}^{(d)*}(\mathbf{r}_d, \boldsymbol{\tau}), \quad (41)$$

where the lack of $\boldsymbol{\tau}$ on the left-hand side implies a sum over the source.

E. Label-free transfer functions

Combining Equations 39–40 and applying a 3D Fourier transform yields

$$E_i^{(d)}(\mathbf{v}, \boldsymbol{\tau}) = P_{ij}(\mathbf{v}) \left[G_{jn}(\mathbf{v}) F_{nk}(\mathbf{v} - \boldsymbol{\tau}) + \delta_{jk} \delta(\mathbf{v} - \boldsymbol{\tau}) \right] S_k(\boldsymbol{\tau}), \quad (42)$$

where capital letters denote 3D Fourier transforms. Similarly, Equation 41 becomes

$$\Phi_{ii'}^{(d)}(\mathbf{v}) = E_i^{(d)}(\mathbf{v} - \mathbf{v}', \boldsymbol{\tau}) E_{i'}^{(d)*}(-\mathbf{v}', \boldsymbol{\tau}) \equiv \left[E_i^{(d)} \star E_{i'}^{(d)} \right](\mathbf{v}), \quad (43)$$

where \star is a shorthand for 3D autocorrelation.

Plugging Equation 42 into Equation 43 and expanding terms yields

$$\begin{aligned} \Phi_{ii'}^{(d)}(\mathbf{v}) = & P_{ij}(\mathbf{v} - \mathbf{v}') G_{jn}(\mathbf{v} - \mathbf{v}') F_{nk}(\mathbf{v} - \mathbf{v}' - \boldsymbol{\tau}) S_k(\boldsymbol{\tau}) P_{i'j'}^*(-\mathbf{v}') \delta_{j'k'} \delta(-\mathbf{v}' - \boldsymbol{\tau}) S_{k'}^*(\boldsymbol{\tau}) + \\ & P_{ij}(\mathbf{v} - \mathbf{v}') \delta_{jk} \delta(\mathbf{v} - \mathbf{v}' - \boldsymbol{\tau}) S_k(\boldsymbol{\tau}) P_{i'j'}^*(-\mathbf{v}') G_{jn}^*(-\mathbf{v}') F_{nk'}^*(-\mathbf{v}' - \boldsymbol{\tau}) S_{k'}^*(\boldsymbol{\tau}) + \\ & P_{ij}(\mathbf{v} - \mathbf{v}') \delta_{jk} \delta(\mathbf{v} - \mathbf{v}' - \boldsymbol{\tau}) S_k(\boldsymbol{\tau}) P_{i'j'}^*(-\mathbf{v}') \delta_{j'k'} \delta(-\mathbf{v}' - \boldsymbol{\tau}) S_{k'}^*(\boldsymbol{\tau}) \end{aligned} \quad (44)$$

and a small scatter-scatter term, which we ignore for weakly scattering objects. Integrating with respect to $\boldsymbol{\tau}$, reducing the Kronecker deltas, and swapping k and k' in the second term yields

$$\begin{aligned} \Phi_{ii'}^{(d)}(\mathbf{v}) = & P_{ij}(\mathbf{v} - \mathbf{v}') G_{jn}(\mathbf{v} - \mathbf{v}') P_{i'k'}^*(-\mathbf{v}') S_{k'}^*(-\mathbf{v}') S_k(-\mathbf{v}') F_{nk}(\mathbf{v}) + \\ & P_{ik'}(\mathbf{v} - \mathbf{v}') S_{k'}(\mathbf{v} - \mathbf{v}') S_k^*(\mathbf{v} - \mathbf{v}') P_{i'j'}^*(-\mathbf{v}') G_{jn}^*(-\mathbf{v}') F_{nk}^*(\mathbf{v}) + \\ & P_{ik}(\mathbf{v} - \mathbf{v}') P_{i'k'}^*(-\mathbf{v}') S_k(-\mathbf{v}') S_{k'}^*(-\mathbf{v}') \delta(\mathbf{v}). \end{aligned} \quad (45)$$

Finally, substituting our 3D autocorrelation shorthand gives the key result

$$\begin{aligned} \Phi_{ii'}^{(d)}(\mathbf{v}) = & \left[P_{ij} G_{jn} \star P_{i'k'} S_{k'} S_k^* \right](\mathbf{v}) F_{nk}(\mathbf{v}) + \\ & \left[P_{ik'} S_{k'} S_k^* \star P_{i'j'} G_{jn} \right](\mathbf{v}) F_{nk}^*(\mathbf{v}) + \\ & \left[P_{ik} \star P_{i'k'} S_{k'}^* S_k \right](\mathbf{v}) \delta(\mathbf{v}), \end{aligned} \quad (46)$$

which provides a linear relationship between the permittivity tensor spectrum $F_{nk}(\mathbf{v})$ (and its conjugate $F_{nk}^*(\mathbf{v})$) and the polarization matrix spectrum $\Phi_{ii'}^{(d)}(\mathbf{v})$ in terms of autocorrelated pupils and Green's tensor spectra.

We can now express the relationship between the Stokes spectra $D_c(\mathbf{v})$ and the scattering potential tensor expansion coefficient spectra $\left[\mathfrak{F}_{\ell m}^{(\text{lf, re})}(\mathbf{v}), \mathfrak{F}_{\ell m}^{(\text{lf, im})}(\mathbf{v}) \right]$ with transfer functions

$$D_c(\mathbf{v}) = + H_{c\ell m}^{(\text{lf, re})} \mathfrak{F}_{\ell m}^{(\text{lf, re})}(\mathbf{v}) + H_{c\ell m}^{(\text{lf, im})} \mathfrak{F}_{\ell m}^{(\text{lf, im})}(\mathbf{v}) + b_c \delta(\mathbf{v}), \quad (47)$$

where the transfer functions are given by

$$\begin{bmatrix} H_{c\ell m}^{(\text{lf, re})} \\ H_{c\ell m}^{(\text{lf, im})} \end{bmatrix} = c_{ii'} \begin{bmatrix} 1 & 1 \\ i & -i \end{bmatrix} \left[\left[P_{ij} G_{jn} \star P_{i'k'} S_{k'} S_k^* \right](\mathbf{v}) \right] \mathcal{Y}_{\ell m}^{nk} \quad (48)$$

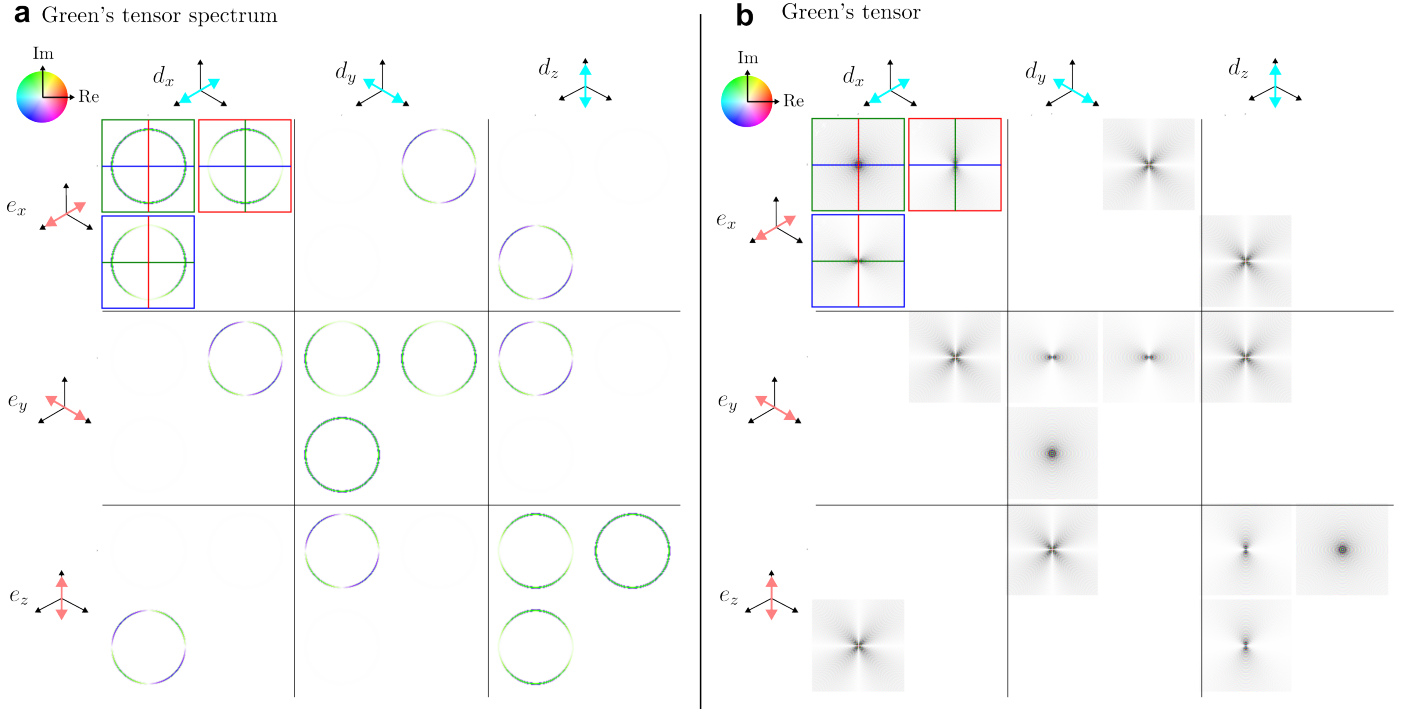


Fig. 8. Orthogonal slices through the **(a)** Green's tensor spectrum $G_{ij}(\nu)$ and the **(b)** Green's tensor $g_{ij}(\mathbf{r})$. The Green's tensor describes the electric field components e_x , e_y , and e_z scattered by a dipole oriented along \hat{x} , \hat{y} , \hat{z} . The Green's tensor spectrum is illustrated in 3D in **Figure 1(b)**.

$$b_c = \sigma_c^{ii'} [P_{ik} \star P_{i'k'} S_k^* S_{k'}] (\nu). \quad (49)$$

This vector model reduces to earlier scalar models [15, 47, 48] by removing the indices from the illumination and detection models (a scalar model assumes no cross terms between field components) and assuming the Green's tensor spectrum is the identity (a good approximation for an isotropic scatterer). **Supplement Figure 9** shows orthogonal sections through low- and high-NA label-free transfer functions for phase and transverse birefringent objects.

F. Fluorescence forward model

We ignore the effects of illumination (and its potential to alias higher frequencies into the pass band of the detection arm) to simplify and to allow us to focus on the similarities and differences between label-free and fluorescence transfer functions.

Starting with a set of incoherent dipole emitters $f_k^{(fl)}(\mathbf{r}_o)$, we can model the fields that reach the detector from a single object point \mathbf{r}_o with a double convolution

$$e_i^{(d)}(\mathbf{r}_d, \mathbf{r}_o) = p_{ij}(\mathbf{r}_d - \mathbf{r}'_o) g_{jk}(\mathbf{r}'_o - \mathbf{r}_o) f_k^{(fl)}(\mathbf{r}_o), \quad (50)$$

where p_{ij} is the detection pupil and g_{jk} is the Green's tensor.

Similar to the label-free case, we can calculate the observables by taking the outer product of the fields

$$\phi_{ii'}^{(d)}(\mathbf{r}_d) = e_i^{(d)}(\mathbf{r}_d, \mathbf{r}_o) e_{i'}^{(d)*}(\mathbf{r}_d, \mathbf{r}_o), \quad (51)$$

but here the lack of \mathbf{r}_o on the left-hand side implies a sum over the sample instead of the label-free sum over source.

G. Fluorescence transfer functions

Combining **Equations 50–51** yields

$$\phi_{ii'}^{(d)}(\mathbf{r}_d) = p_{ij}(\mathbf{r}_d - \mathbf{r}'_o) g_{jk}(\mathbf{r}'_o - \mathbf{r}_o) p_{i'j'}^*(\mathbf{r}_d - \mathbf{r}'_o) g_{j'k'}^*(\mathbf{r}'_o - \mathbf{r}_o) f_k^{(fl)}(\mathbf{r}_o) f_{k'}^{(fl)*}(\mathbf{r}_o), \quad (52)$$

and taking a Fourier transform results in

$$\Phi_{ii'}^{(d)}(\nu) = P_{ij}(\nu - \nu') G_{jk}(\nu - \nu') P_{i'j'}^*(-\nu') G_{j'k'}^*(-\nu') F_k^{(fl)}(\nu) F_{k'}^{(fl)*}(\nu). \quad (53)$$

Expanding onto our object- and data-space bases results in the model

$$D_c(\nu) = H_{c\ell m}^{(fl)}(\nu) \mathfrak{F}_{\ell m}^{(fl)}, \quad (54)$$

where

$$H_{c\ell m}^{(fl)}(\nu) = \sigma_k^{ii'} [P_{ij} G_{jk} \star P_{i'j'} G_{j'k'}] (\nu) \mathcal{Y}_{\ell m}^{kk'}. \quad (55)$$

18. SUPPLEMENT: ARCHITECTURE OF WAVEORDER AND RECORDER

waveOrder is organized into a list of contrast modes named using the schema:

<object-type>_<sample-thickness>_<data-type>_<optics-model>.

<object-type> can take the values

- `inplane_oriented`, to indicate phase and transverse-birefringent objects
- `phase`, to indicate phase-only objects,
- `isotropic`, to indicate phase and absorption objects,
- `isotropic_fluorescent`, to indicate isotropic fluorescent dipoles.

<sample-thickness> can take the value `thin` and `thick` to indicate the dimension of the reconstruction.

<data-type> can take the value `3d` to indicate unpolarized data and `pol3d` to indicate Stokes data.

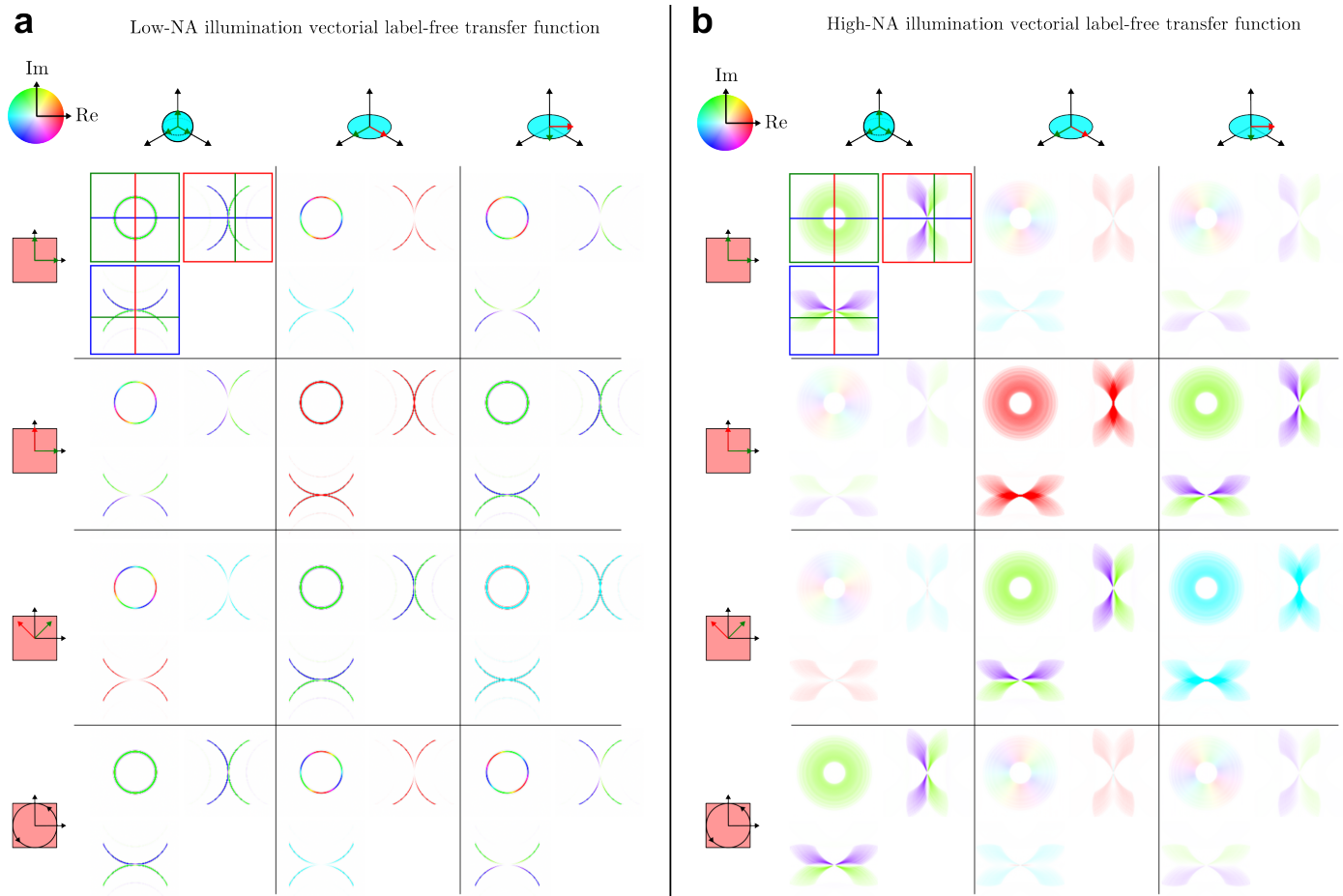


Fig. 9. Phase and birefringence transfer functions $H_{\ell m}^{k(\text{lf, re})}(\nu)$, $\text{NA}_{\text{det}} = 1.2$ and **(a)** $\text{NA}_{\text{ill}} = 0.01$ and **(b)** $\text{NA}_{\text{ill}} = 0.5$. **Rows** correspond to Stokes parameters $c = [0, 1, 2, 3]$ and **columns** correspond to material properties $(\ell, m) = [(0, 0), (2, -2), (2, 2)]$. Here the index of refraction $n = 1.3$.

`<optics-model>` can be empty, indicating scalar models with some ray-optics assumptions, or vector indicating full vector optics models.

The currently implemented contrast modes are

- `inplane_oriented_thick_pol3d`,
- `inplane_oriented_thick_pol3d_vector`,
- `phase_thick_3d`,
- `isotropic_thin_3d`,
- `isotropic_fluorescent_thick_3d`,

and we anticipate future contrast modes with larger and more varied subsets of the 18 label-free and 9 fluorescence parameters described within the waveOrder framework.

Each contrast mode includes the following methods:

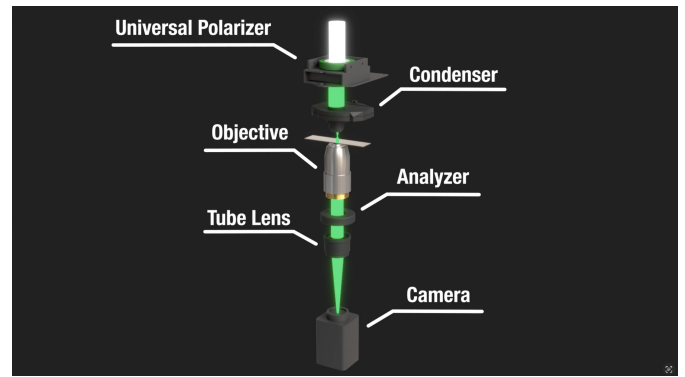
- `generate_test_phantom`,
- `calculate_transfer_function`,
- `visualize_transfer_function`,
- `apply_transfer_function`,
- `apply_inverse_transfer_function`.

All waveOrder functions are implemented as python methods with PyTorch Tensor objects as input and output. We enable applications that require reconstructions from and to files on disk via a separate repository, `recOrder`, which includes a command-line interface (CLI) and a napari plugin for reconstructing material properties from multi-contrast multi-channel data. `recOrder`'s CLI uses configuration files to specify details about each contrast type, and it includes the following commands

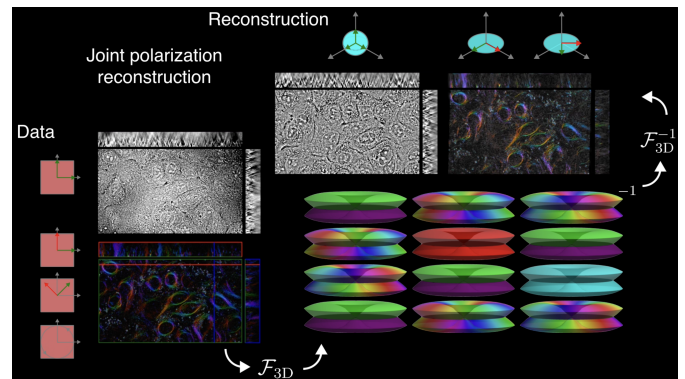
- `reconstruct`, for an end-to-end reconstruction,
- `compute-tf`, for precomputing transfer functions, often the most expensive part of the reconstruction, and
- `apply-inv-tf`, for applying a precomputed transfer function to a dataset.

All of `recOrder`'s file I/O is in the OME-Zarr format, enabled by the `iohub` library.

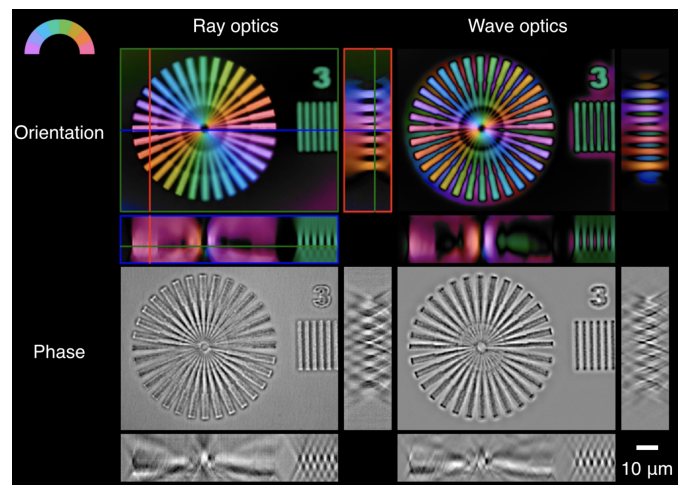
19. SUPPLEMENT: VIDEOS



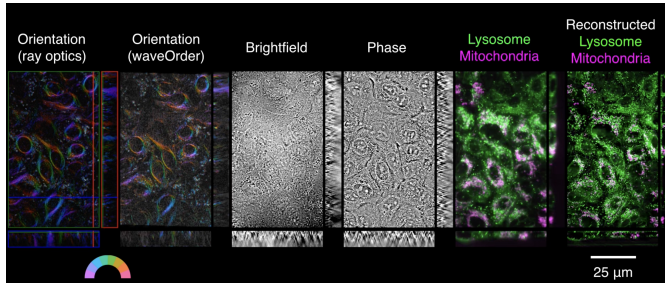
Video 1. Animation illustrating polarized illumination label-free acquisitions. A pair of liquid crystals [0:00–0:10] form a universal polarizer as part of a complete imaging system [0:10–0:25]. Defocus volumes under different polarized illuminations form complete datasets [0:25–0:45], which are used to reconstruct retardance, orientation, and phase [0:45–1:04].



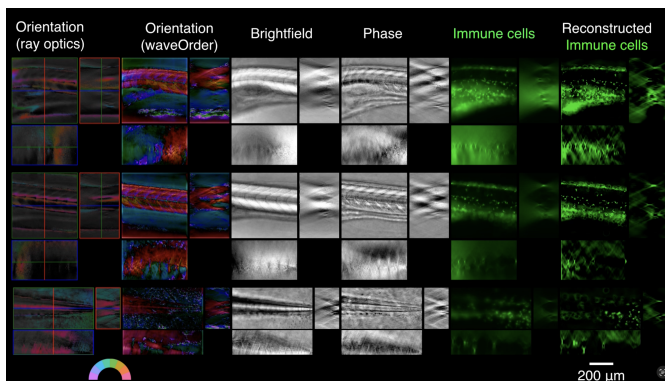
Video 2. Animation illustrating through-focus sweeps of data, optical transfer functions, and reconstructions for fluorescence deconvolution [0:00–0:07], phase from brightfield [0:07–0:15], and joint polarization reconstructions [0:15–0:25].



Video 3. Through-focus sweep of spoke target data and reconstruction, corresponding to Figure 3c.



Video 4. Through-focus sweep of A549 cell data and reconstruction, corresponding to **Figure 4a**.



Video 5. Through-focus sweep of zebrafish tissue data and reconstruction, corresponding to **Figure 4c-e**.